UNIVERSITY OF SOUTHAMPTON

SCHOOL OF ENGINEERING SCIENCES

FACULTY OF ENGINEERING, SCIENCES AND MATHEMTICS

Aerodynamics of F1 Car Side Mirror

By

E. Rind and Z. W. Hu

Report No. AFM-07/06

2007

Aerodynamics of F1 Car Side Mirror

E. Rind and Z. W. Hu

Abstract

This study investigates the aerodynamic performance of a Formula 1 car rear view side mirror when the location of its glass is varied inside its frame. Both experimental and computational studies have been carried out for a simplified two-dimensional model of a typical Formula 1 mirror at different Reynolds numbers. Experimental results showed strong correlation between the mirror's glass location and its drag over all investigated Reynolds number range of 1.1×10^5 to 2.6×10^5 – as the mirror's glass is located further inside its frame a reduction in the drag is achieved with a maximum of 10%-11%. No change is found in the mirror's vortex shedding frequency at all investigated Reynolds numbers which implies no structural impact of this modification. However the computational results obtained using Fluent failed to predict the changes in flow characteristics and drag caused by the proposed modification, more calculations are needed using higher order numerical methods should be performed to investigate this phenomenon further to confirm the experimental findings.

1. Introduction

Aerodynamics always plays a major role in Formula 1 (F1) car's performance. In the early days of race car history, most of the aerodynamic work was concentrated in reducing the car's drag. That is why the first F1 cars had a streamlined shape – narrow front and rear parts of the body and smooth body work. Later on, as engines became more and more powerful, car design concentrated more on achieving greater cornering performance and stability. It started with work on the car's suspension and its central of gravity, but the most significant progression came from the generation of downforce which started with the introduction of the front and rear wings in 1967 whose effects was later enhanced by the finding of ground effect in 1977. Restriction on engine size put forward in 2006 by the Fédération Internationale de l'Automobile (FIA) brought back the importance of the drag's influence on the cars' performance.

In general the entire car is designed for aerodynamic performance. The rear view side mirror (RVSM) is one of the most difficult parts as it has to be in particular place due to safety regulations. They are bluff bodies and their shape, no matter how it is modified, generates large percentage of the car's total drag. For example in road cars, the RVSMs generate 5% of the total drag of the car, in spite of their area being nowhere near 5% of the total cross sectional area [17]. Moreover, the RVSM has a large negative influence on other car parts due to its wake and vortex shedding.

This research concentrates on the influence of the location of RVSM's glass inside its frame on the mirror's aerodynamic performance. In general the flow around a RVSM is three-dimensional and is very complicated. A simplified two-dimensional model was used for this study. Since the outer shape of the mirror frame is similar to an elongated half cylinder, it might be helpful to review main flow features around a cylinder and only later to summarize some of the work done on RVSMs.

1.1 Cylinders - Overview

The flow around cylinder can be categorised in several ways according to the shape of the cylinder, the number and arrangement of cylinders or the type of the surroundings in which the cylinders are placed. Figure 1 illustrates some examples.

Many studies have been carried out on circular cylinder. The main reason for this is the complex flow structure around it combined with its simple geometry. Flow around more than one cylinder has also been widely investigated, for example, two cylinders in side by side, tandem or staggered arrangements. This type of research has large interest as it is a basic form of a multi-component cylinder flow. A complete review on this subject was given by Zdravkovich [20]. Cylinder in both unbounded flow and wall-bounded flow demonstrate the different surroundings.

The flow pattern around a cylinder depends not only on the cylinder shape and configuration, but also on a variety of influencing parameters [19]. For example, for a long circular cylinder placed in a uniform cross-flow the dominant influencing parameter is the Reynolds number:

$$Re = \frac{U_\infty d}{\nu},$$

where U_∞ is the freestream velocity, d is the cylinder diameter and ν is the kinematic viscosity of the fluid.

Flow around a circular cylinder can be classified into four primary regimes: sub-critical, critical, super-critical and post-critical regimes. In most practical cases for a F1 car mirror other influencing parameters also have large effect on the flow pattern. Among those parameters are freestream turbulence, surface roughness, aspect ratio of the cylinder and cylinder's oscillation. In the case of wall-bounded flows the gap ratio, $^h/_d$ (h is the gap between the cylinder and the wall and d is the cylinder diameter) also has a significant influence on the flow pattern.

The flow around cylinders can be analysed using both experimental and computational method, as it is done in this research. One of the things that influenced by those parameters is the forces induced on the cylinder by the flow which are usually described by their coefficients –

Drag Coefficient:

$$C_D = \frac{Drag}{^1/_2\,\rho U_\infty^2 A}$$

Lift Coefficient:

$$C_L = \frac{Lift}{^1/_2\,\rho U_\infty^2 A}$$

Those forces might fluctuate mainly due to the vortex shedding. Therefore mean force coefficients (C_{D_0} and C_{L_0}) and Strouhal number are of a major interest in many studies. The Strouhal number is defined as

$$St = \frac{fd}{u_\infty}$$

Where f is the vortex shedding frequency, U_∞ is the freestream velocity and d is the cylinder diameter.

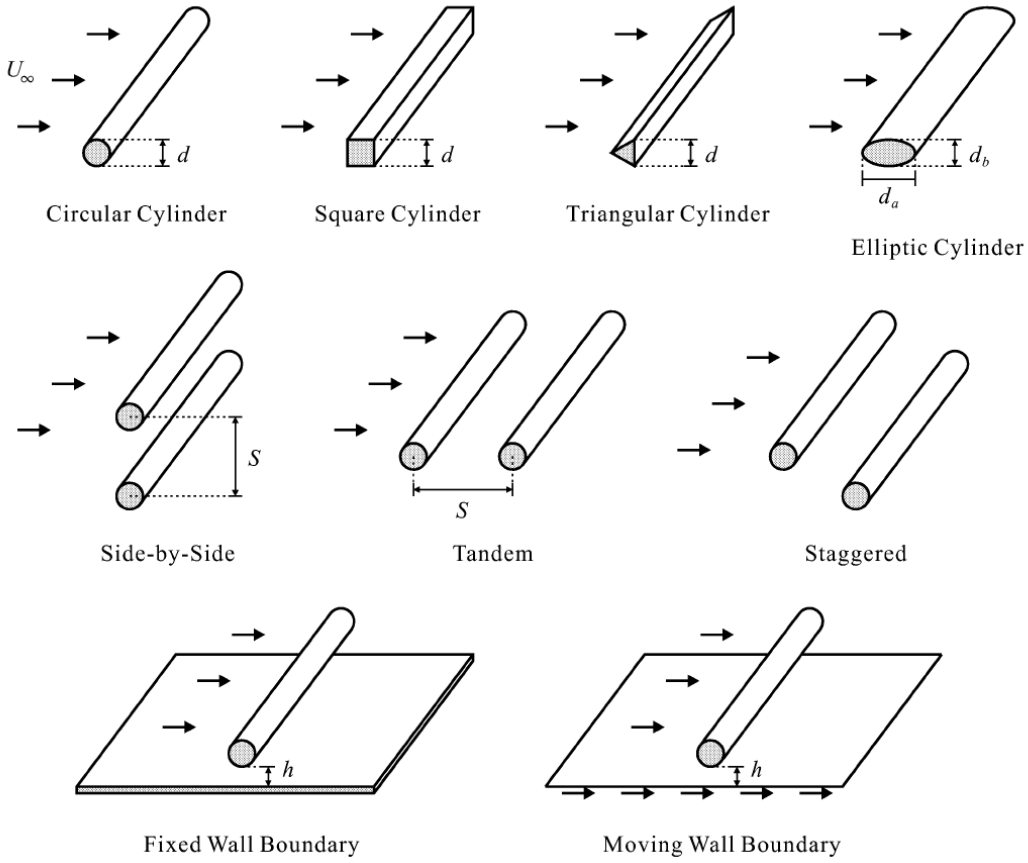

Figure 1 – Examples of flow around cylinders, [15].

1.1.1 Flow Regimes Based on Reynolds Number

It has been noticed at the early stage of the study on flow around circular cylinders more than 100 years ago that the induced force applied on a circular cylinder depends on the flow condition – Reynolds number. The lift and drag coefficients (C_D and C_L respectively) can be expressed as a function of the cylinder diameter Reynolds number, Re_d.

In 1916 Taylor (as mentioned in [19]) found a drastic change in the pressure distribution around a circular cylinder before and after the so called 'critical Reynolds number' - Re_c. Wieselsberger in 1922 (as mentioned in [12]) reported drag measurements on circular cylinders of various diameters and thereby covering Reynolds number from 4×10^5 to 8×10^5, where the drag suddenly decreased around $Re_d = 2 \times 10^5$ - the critical Reynolds number. The pressure distribution on circular cylinders around the critical Reynolds number was further investigated by several other researchers (as mentioned in [12]).

Those early experiments lead to the idea of classifying the flow pattern around a circular cylinder based on the Reynolds number into three fundamental regimes: Sub-critical – $Re_d < Re_C$, Critical - $Re_d \cong Re_C$ and Super-critical – $Re_d > Re_C$. The sub-critical regime is characterized by a laminar boundary layer around the cylinder at low Reynolds numbers ($Re_d < 4 \times 10^4$). At higher Reynolds numbers ($4 \times 10^4 < Re_d < 2 \times 10^5$) which is the upper range of the sub-critical regime the laminar boundary layer separates to form a free shear layer and sudden break into turbulence occurs in the free shear layer close to the cylinder. That free shear layer accumulates and forms large scale vortices and they shed alternately from each side of the cylinder – Karman type vortex shedding. As the Reynolds number gets larger the large scale vortices compose into a wide turbulent wake of statistically periodic vortices and the mean drag coefficient, C_{D_0}, has a relatively constant value near unity. In the critical

regime the transition to turbulence takes place just after the separation and the separated flow reattaches afterwards introducing separation bubbles on the cylinder. This leads to a thinner wake, cessation of the regular vortex shedding, an increase in the base pressure coefficient and therefore the drag coefficient, C_D, of the cylinder drops to about 0.3. In 1969 Bearman [4] found that the regular vortex shedding continues after the critical drop in the pressure coefficient but only up to $Re = 5.5 \times 10^5$, therefore he suggested that the critical regime should end with the cessation of the vortex shedding. In the supper-critical regime which is characterised by the non-existence of the vortex shedding the separation bubbles are irregularly fragmented along the span of the cylinder and drag coefficient slightly recovers as the Reynolds number increases.

It was not until 1961 when Roshko [10] discovered the fourth regime at $Re > 3.5 \times 10^6$ and he named it as the trans-critical regime. Nowadays, this regime is known as post-critical. This regime is characterized with the disappearance of the separation bubbles due to the fact that the transition to turbulence takes place before the separation all along the span of the cylinder. Also, the regular vortex shedding reappears and the wake becomes wider than in the critical and supper-critical regimes (but still narrower than it was in the sub-critical regime). As a result to all mentioned above the drag coefficient becomes larger and has a relatively constant value of 0.7.

Due to substantial differences among the reported experimental data that usually was the result of influencing parameters other than Reynolds number, for example the level of free stream turbulence, aspect ratio of the cylinder etc. Morkovin suggested in 1964 [9] to divide the flow regimes not by a defined Reynolds number at each start and end but using a range of Reynolds numbers for each start and end of each flow regime. Using that method he classified the flow around a circular cylinder into seven different flow regimes.

Zdravkovich [4] defined the flow regimes in terms of where the transition to turbulence takes place. This definition led to five main flow regimes and each was also subdivided into sub regimes as illustrated in Figure 2. The main flow regimes are: fully laminar for $0 < Re < 180 - 200$ denoted by 'L'; transitioning wake – $180 - 200 < Re < 350 - 400$ - 'TrW'; transition in shear layers – $350 - 400 < Re < 10^5 - 2 \times 10^5$ - 'TrSL'; transition in boundary layers – $10^5 - 2 \times 10^5 < Re < 6 \times 10^6 - 8 \times 10^6$ - 'TrBL' and fully turbulent – $Re > 8 \times 10^6$ - 'T'. More detailed definitions of the flow regimes were suggested by many researches during the years, for example Farell in 1981, Roshko in 1993 and Williamson in 1996 (As mentioned in [15]).

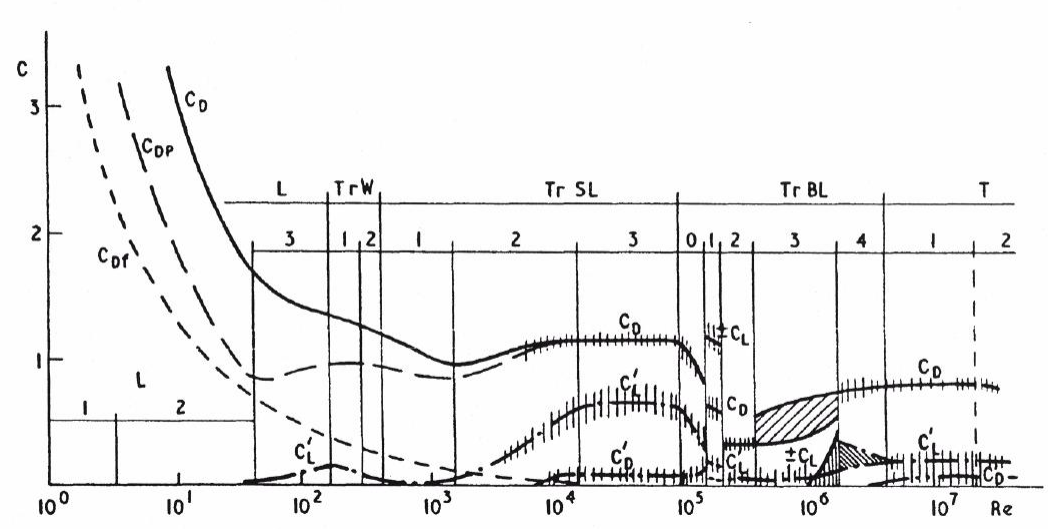

Figure 2 – Drag coefficient for a smooth cylinder as function of Reynolds number in undisturbed flow, [19].

** In Figure 2 C_{Df} is the viscous drag, C_{DP} is the pressure drag and C_D is the total drag. Coefficients for fluctuations in drag and lift coefficients are $C_D^{'}$ and $C_L^{'}$ reprehensively.

1.1.2 Effects of Surface Roughness

While the governing parameter for the state of flow for smooth cylinders is the Reynolds number, surface roughness can lower the Reynolds number at which transition occurs and in some cases govern the state of the flow.

Before considering roughness, the concept of a smooth cylinder warrants some discussion. It is clear that no real object can be perfectly smooth. While a surface may visually appear smooth or feel smooth to the touch, surface irregularities will become apparent under sufficient magnifications. The definition of smoothness should therefore be when the surface irregularities and imperfections are sufficiently small that they have no effect on the flow.

At low Reynolds numbers, when the laminar boundary layer is thick, surface roughness should have little effect. Conversely, the flow should be sensitive to surface roughness at high Reynolds number. This is supported by experimental data, where at low Reynolds numbers the drag coefficient is independent of surface roughness.

The roughness of the cylinders can be defined by the relative roughness - K/d (K is the average height of the excrescences of the cylinder surface and d is the cylinder diameter). In 1929 Fage and Warsap (as mentioned In [20]) showed that the critical Reynolds number decreases as the relative roughness increases. The shift of the critical regime towards lower Reynolds number was also confirmed by the variation of Strouhal numbers - St, where the jump of St indicating the change from the sub-critical to post-critical state, shifted toward lower Re range of the super-critical regime, in which no regular vortex shedding occurs, was significantly reduced as K/d is increased. The shift of the critical regime was also shown by Achenbach [1] who measured the pressure coefficient and skin friction coefficient distributions on a circular cylinder and estimated the positions of transition and separation of the boundary layer on the cylinder.

1.1.3 Effects of Free Stream Turbulence

Free steam turbulence has a similar effect to the surface roughness in lowering the transition Reynolds number. Free stream turbulence is defined by the intensity, T_i, and a length scale, T_s. Turbulence intensity is the ratio of the root-mean-square fluctuation velocity to the time-averaged velocity. Integral turbulence length scale is an estimate of the size of the dominant eddies, and is calculated from the spatial correlation function of the velocities in the streamwise direction. Of the two, turbulence intensity appears to have a greater effect on cylinder flow [18].

In the TrSL3 (See Figure 2) regime, in which the current study was taking place based on Reynolds number, where there is an abrupt transition to turbulence in the free-shear layers, the effect of free-stream turbulence is confined to the short section of laminar flow in the shear layer (upstream of the transition point). This short length scale means that the turbulence length scale must be small for free-stream turbulence to have an effect (Surry [14]).

1.1.4 Effects of Cylinder Aspect Ratio and End Condition

A very important parameter that should be taken into account in any experiment involving cylinders is the aspect ratio of the cylinder - l/d, where l is the length of the cylinder, and the end conditions of the cylinder. The end conditions can be categorised into three groups: free ends, close ends and ends equipped with end plates.

In the case of free ends, the cylinder is isolated in the fluid flow and not connected to walls/plates, the aspect ratio of the cylinder has a major effect on the characteristics of the flow and the force acting on it due to the edge vortices. In order to achieve flow without free ends effects, two dimensional, the aspect ratio of the cylinder should be extremely large. In [15] it is mentioned that Fox Et Al reported in 1993 that the free ends effect could extend to a distance of 20 cylinder diameters from the free ends.

In the case for closed ends where the cylinder is connected to the test section walls, the flow and the force characteristics are also affected by the aspect ratio of the cylinder. This is due to the horseshoe vortices generated around the closed ends due to the boundary layer developed on the test section ends (Baker [2]). Baker also reported that the horseshoe vortices may disturb the two-dimensionality of the flow when the aspect ratio of the cylinder is not large enough.

The case of ends equipped with end plates is similar to the closed ends case apart from the advantage that the boundary layer on the end plates is smaller than that on the test sections. Szepessy and Bearman [11] reported that the effect of the aspect ratio is very large and is Reynolds number dependent. The use of appropriate end plates can lower the aspect ratio to achieve 2-D flow which is needed at Reynolds number range of $2 \times 10^4 < Re < 10^5$.

1.2 Rear View Side Mirror

Rear view side mirrors (RVSMs) contribute significantly to the car's drag. They are a protrusion on the car's body which produce wakes behind them. The wake can be resembled to the wake of a semi-sphere. When reaching the RVSM, the air goes around the edges and encounters a very high adverse pressure gradient and the flow separates. In some RVSMs the proximity of the body of the car will even slow the fluid more and increase the wake.

The RVSM design should consider two aspects: the driver's ability to see properly the surroundings behind the car, and the RVSM influence on the car's performance. These lead to many design limitations due to safety issues which obviously affects its influence on the cars' performance.

The RVSM has a large interest now not only in autosport for improving the cars' performance, but also in the production car industry for improving the cars' efficiency. In F1, as the cars get more uniform in appearance and performance due to regulations the focus during the years has changed towards smaller improvements that can put the team in the winner's circle. As for the efficiency and fuel consuming of the cars, that had no real meaning in F1 but it is one of the main interests nowadays in the automotive industry due to global warming and high fuel rates.

The trend in RVSM design of race car is to streamline the shape and by that reducing its drag resulting by weight reduction. Streamlining of the mirror is done from the concept of making the front part of the mirror resemble a droplet of water with consideration of not disturbing the flow over the entire car and not creating excessive weight in the process. The limitation is the demand of having a sufficient mirror area in order to have the desired and necessary view field.

2. Methodology

This research is to study the aerodynamic performance of a RVSM when the mirror's glass location inside the frame is altered. The reasoning is that as the mirror's glass is located further inside the frame the wake behind it will be closed due to the 'suction' behind the mirror. This, hopefully, will

reduce the wake resulting reduction of the mirror's drag and also will help to improve downstream elements' aerodynamic performance.

The investigation has been done both experimentally and computationally using a simplified 2D model to achieve some fundamental understandings of the modification's influence. The main parameters checked during the investigation are the mirror's drag coefficient, vortex shedding frequency, the mean flow field of the near wake of the mirror and the wake's width and energy downstream to the mirror. Experimental and computational studies have been carried out for mean drag measurements, visualization of the near wake using Particle Image Velocimetry (PIV), energy spectra and vortex shedding frequency measurements using Hot Wire Anemometry (HWA) and averaged velocity sampling downstream the mirror inside its wake using a Pitot-tube.

2.1 Model Design

The first parameter determined for the 2D model is the mirror's diameter. FIA regulations require $d = 0.07[m]$. Since F1 car drives in an average speed of $55\ [^{m}/_{sec}]$ which is higher than the wind tunnel's maximum speed of $45[^{m}/_{sec}]$. The mirror diameter was decided to achieve Reynolds number similarity at wind tunnel speed limitation as illustrated bellow.

- Reynolds number for F1 mirror

$$Re = \frac{U_\infty d}{\nu} = \frac{55 \times 0.07}{1.46 \times 10^{-5}} = 2.6 \times 10^5$$

- By the condition of Reynolds number similarity the wind tunnel model's diameter should be $d = 0.085[m]$

The mirror shape was decided to be an elongated half cylinder with rectangular dint in its trailing edge as shown in Figure 3. Due to practical reasons Reynolds number similarity is not calculated at the PIV's velocity limitation of $20[^{m}/_{sec}]$ otherwise the mirror size would have been very large and also the accompanying parts – endplates etc (for example the mirror diameter would have been 0.1925[m]). The Reynolds number at $20[^{m}/_{sec}]$ is also calculated for the endplates and the mirror's aspect ratio as illustrated bellow.

$$Re = \frac{U_\infty d}{\nu} = \frac{20 \times 0.085}{1.46 \times 10^{-5}} \cong 1.1 \times 10^5$$

The endplate size and the mirror aspect ratio were decided according to Szepessy and Bearman [11] based on the mirror's diameter and the working Reynolds number ($Re = 1.1 \cdot 10^5$). The endplates are rectangular plates $8d$ long and $7d$ wide. Since PIV was used the endplates had to be made out of a high quality transparent material Cast Clear Acrylic is used. The distance between the mirror axis and the leading edge of the endplates is $3.5d$ (the mirror axis is located in the centre on the half cylinder – leading edge of the mirror). The aspect ratio is 7, therefore the mirror length is $0.6[m]$.

Figure 3 – Side view of the mirror's wind tunnel model.

HWA has also been used to measure the vortex shedding behind the mirror. It is necessary to build a bridge above the model so as to locate the hotwire $2d$ downstream of the model and also the hotwire height could be changed to measure at the upper boundary of the wake. The wake velocity profile is measured with a Pitot tube placed 14.1 diameters behind the mirror. A supporting beam is designed to connect the Pitot tube to a height control system moving it across the wake.

All the parts were designed using the commercial CAD package Solid Edge based to fit in to the wind tunnel's force balance and the height control system. Detailed CAD drawings are attached in Appendix C.

2.2 The Wind Tunnel

The University of Southampton $7' \times 5'$ closed circuit wind tunnel was used for this research. Because a F1 car's mirror is not affected by the ground the moving ground facility was not used. For the purpose of this study the moving ground was covered with a wooden horizontal plane. Details of the wind tunnel can be found in [16].

2.3 Measurement Tools

2.3.1 Balance for Drag Measurements

The Balance was used to sample time-averaged force measurements at different Reynolds numbers and mirror configurations. First the drag measurements were taken with only the endplates and the balance's struts for calibration purposes, only then the entire model mirror is installed and drag for the entire set is recorded. The drag for the mirror is the subtraction of the two.

2.3.2 Particle Image Velocimetry (PIV) System and Its Settings

A Dantec FlowMap 2D-PIV system (PIV2100) is used for all PIV measurements. A double-pulse Nd:YAG laser was located approximately $2.5m$ downstream of the of the mirror's centre, as can be seen in Figure 4, to create a laser sheet of about 4mm thick, lighting the mid-span, x-y plane behind the mirror (downstream). Smoke particles with a diameter of approximately $1[\mu m]$ were used as the seeding. The smoke machine was located downstream the wind tunnel, as can be seen in Figure 5, such that when the smoke is released it has enough time to effectively mix within the air as the wind tunnel used is closed circuit (See 2.2).

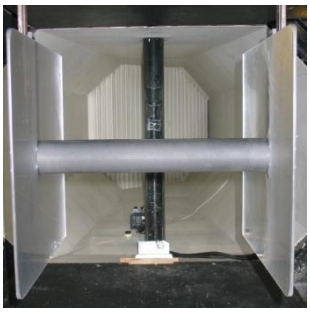

Figure 4 – Laser located downstream the mirror.

Figure 5 - The smoke machine downstream the wind tunnel.

The illuminated particle images were captured using a Dantec HiSense CCD camera (1280×1024 pixels, 8bits/pixel) with a $62[mm]$ length, which was synchronized with the laser so as to implement the so-called 'double frame/single exposure' recording. The camera was located outside the wind tunnel such that it captures the laser sheet, as can be seen in Figure 6. The time delay between two laser pulses was set at $15[\mu s]$ and 500 pairs of images were continuously recorded for each experimental flow and setup condition with a sampling rate of $2Hz$ which is not high enough to resolve the time evolution of the vortex shedding behind the mirror, which was then measured by HWA.

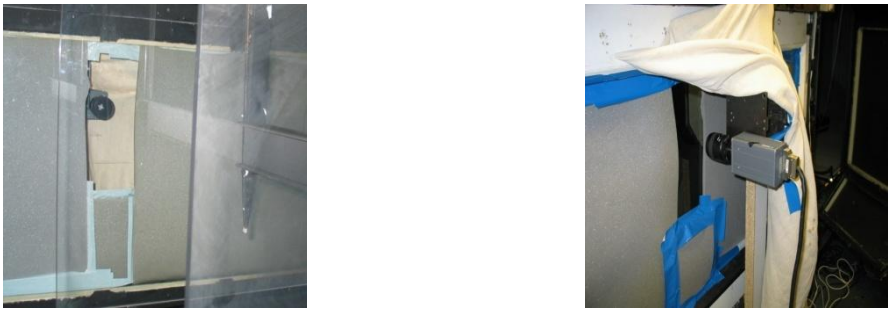

Figure 6 - CCD camera located outside the wind tunnel (left: inside view; right: outside view).

Each pair of images recorded was then analyzed using the cross-correlation technique with an interrogation area of 32×32 pixels with 50% overlapping in both horizontal and vertical directions. The resulting vectors were validated by the correlation-peak-height, velocity range and moving-average validations at that order. The rejected vectors were replaced with interpolated values from the surrounding valid vectors in 3×3 point regime, to with no filtering was applied. The obtained 500 instantaneous vector fields were then averaged to yield time averaged flow field data.

2.3.3 Hot Wire Anemometry (HWA) System and Its Settings

The HWA measurements were done using a Dantec How Wire SN 9055P0161 which was located $2d$ downstream of the mirror T.E. in the upper boundary of the wake perpendicular to the freestream to capture the vortex shedding frequency, as can be seen in Figure 7. The analog signal was digitized using IOtech Analog – Digital Converter (ADC488/8SA) to be recorded by computer software.

For each case 100 blocks of data were taken. Each block contained 8192 samples. The sampling frequency was $5000[Hz]$. The bridge resistance was set to be $26.7[\Omega]$ based on the hot wire and the cable resistance of $18[\Omega]$.

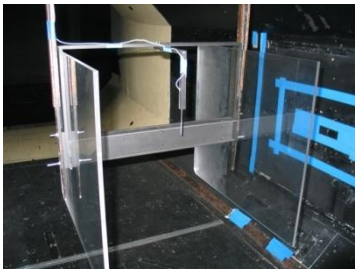

Figure 7 - The Hot Wire setting in the wind tunnel.

This study only interested in the energy spectra from hot wire measurement, therefore no calibration is needed since it is not affected by the absolute values.

2.3.4 Pitot – Static Tube System and Its Settings

The Pitot-static tube measurements were done using a Pitot-static tube and Nutem Betz gate model number – 0112M. The Pitot-static tube was placed 14.1 mirror's diameters downstream to the mirror pointing towards its centre, the tube was connected to the traverse system using the beam that was specially designed for that purpose (See 2.1), as can be seen in Figure 8.

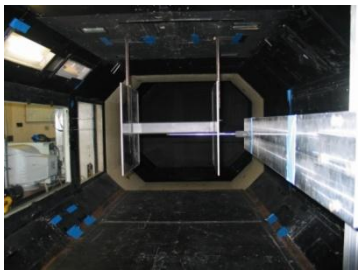
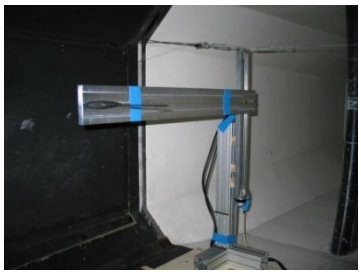

Figure 8 - The pitot-static tube downstream of the mirror (left) and the traverse system (right).

During the measurements it was noticed that the traverse system vibrates. This vibration affects the Betz gate readings. Due to that fact it was decided to stiff the system in order to minimize the effect and do the measurements again which consumes a lot of time. It was also noticed that as the Reynolds number gets higher the vibration of the system becomes stronger therefore the measurement was only carried out at the lowest Reynolds number.

2.3.5 Model Setup and Experimental Procedure

The model was installed in the centre of the test section to the wind tunnel's balance as can be seen in Figure 9.

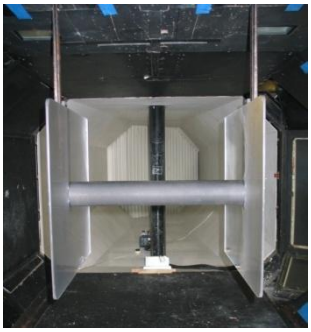

Figure 9 – The mirror installed in the wind tunnel.

Tests have been carried out for six different configurations of the mirror's glass at different flow conditions, as shown in Table 1.

Method	Freestream velocity	Reynolds Number
PIV	$20[^{m}/_{sec}]$	$1.1 \cdot 10^5$
HWA	$20[^{m}/_{sec}]$ $25[^{m}/_{sec}]$ $30[^{m}/_{sec}]$ $35[^{m}/_{sec}]$ $40[^{m}/_{sec}]$ $45[^{m}/_{sec}]$	$1.1 \cdot 10^5$ $1.4 \cdot 10^5$ $1.7 \cdot 10^5$ $2.0 \cdot 10^5$ $2.3 \cdot 10^5$ $2.6 \cdot 10^5$
Force Measurements	$20[^{m}/_{sec}]$	$1.1 \cdot 10^5$

	$25[^{m}/_{sec}]$	$1.4 \cdot 10^5$
	$30[^{m}/_{sec}]$	$1.7 \cdot 10^5$
	$35[^{m}/_{sec}]$	$2.0 \cdot 10^5$
	$40[^{m}/_{sec}]$	$2.3 \cdot 10^5$
	$45[^{m}/_{sec}]$	$2.6 \cdot 10^5$
Pitot-Tube Measurements	$20[^{m}/_{sec}]$	$1.1 \cdot 10^5$

Table 1 - Flow conditions for each preformed test.

2.3.6 Uncertainties in Measurements

Due to the fact that each measurement was taken during a long period of time (10-40 minutes each) and lack of cooling system in the wind tunnel the air temperature rose during each measurement. This affects the air density and also the dynamic pressure. In addition, the ambient pressure was also noticed to be changing during each experiment. All those changes affect the Reynolds number at which the experiment was done. The changes in the Reynolds number were found to be less than 1.5%.

In addition, uncertainties in distances were also noticed. Regarding to the mirror's configuration $\pm 0.2[mm]$ uncertainty was noticed – design tolerance, and regarding to the Pitot - static tube location $\pm 0.35[mm]$ uncertainty was noticed.

Regarding to the Pitot – static tube measurements due to the vibration of the construction holding the tube some oscillation in the measurements was noticed during the readings and they were averaged. The error in the readings is estimated as $\pm 0.3[mmH2O]$. This is equivalent to 2% error.

3. Results and Analysis

Several experiments at different Reynolds Numbers were done using PIV to visualize the flow in the close wake regime downstream of the mirror, HWA was used to extract the energy spectra at a fixed point in the shear layer between the wake and the freestream, Balance to measure the mirror's drag and a Pitot-tube to measure the velocity profile at $^{h}/_{d} = 14.1$ downstream of the mirror.

3.1 Dimensionless Coefficients and Reference Values

In this investigation dimensionless coefficients were used. The coefficients are defined in the following way:

- Drag coefficient - $C_D = \frac{Drag}{^{1}/_{2}\rho U_\infty^2 A}$
- Normalized recirculation length - $R_l = \frac{Recirculation \quad Lengt\ h}{d}$
- Normalized mirror's glass location - $L = \frac{Mirror \ \ Glass \ \ Location}{d}$ (relatively to the T.E.)

The following reference values were used in the normalization process for the current investigation:

- ρ – calculated using the temperature and the ambient pressure during the experiments using the equation of state of a classical ideal gas in the following way:

$$\rho = \frac{P}{R \cdot T}$$

- U_∞ - calculated using the dynamic pressure during the experiment and the calculated density in the following way:

$$U_\infty = \sqrt{\frac{2 \cdot q}{\rho}}$$

- $d = 0.085[m]$
- $l = 0.6[m]$
- $A = l \cdot d = 0.6 \cdot 0.085 = 0.051\ [m^2]$
- $R = 287\left[{}^{J}/_{kg \cdot K}\right]$

3.2 Instantaneous Flow Pattern

PIV measurements of the instantaneous flow field are analysed to investigate wake characteristics behind the mirror. It was noticed that vortices are shed alternatively from each side of the mirror which lead to a flapping motion of the wake, as can be seen in Figure 10, where instantaneous flow field in successive time instants are given with a time interval of 0.5 second.

It is noticed that the wake structure is not exactly like Karman type vortex shedding but a turbulent wake with alternatively vortex shedding which implies similarity to the flow characteristics of the upper sub-critical regime and the critical regime for a circular cylinder. Since the measured drag coefficient was approximately constant for $1.1 \cdot 10^5 < Re < 2.3 \cdot 10^5$ (Figure 11) this might also imply a similarity to the upper sub-critical regime but a firm statement couldn't be drawn due to the lake of information about the boundary layer on the mirror's face and also due to the low number of drag samples. The small drop in the drag coefficient that occurs around $Re \approx 2.5 \cdot 10^5$ might imply the beginning of the critical regime but again a more accurate statement couldn't be done, more measurements in higher Reynolds numbers are needed to conclude on this point.

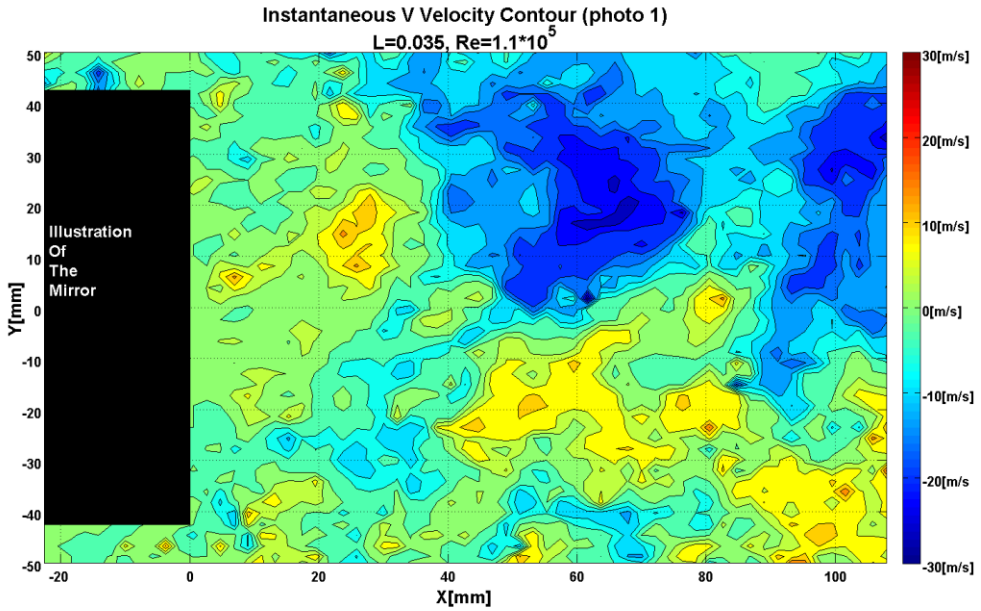

(a)

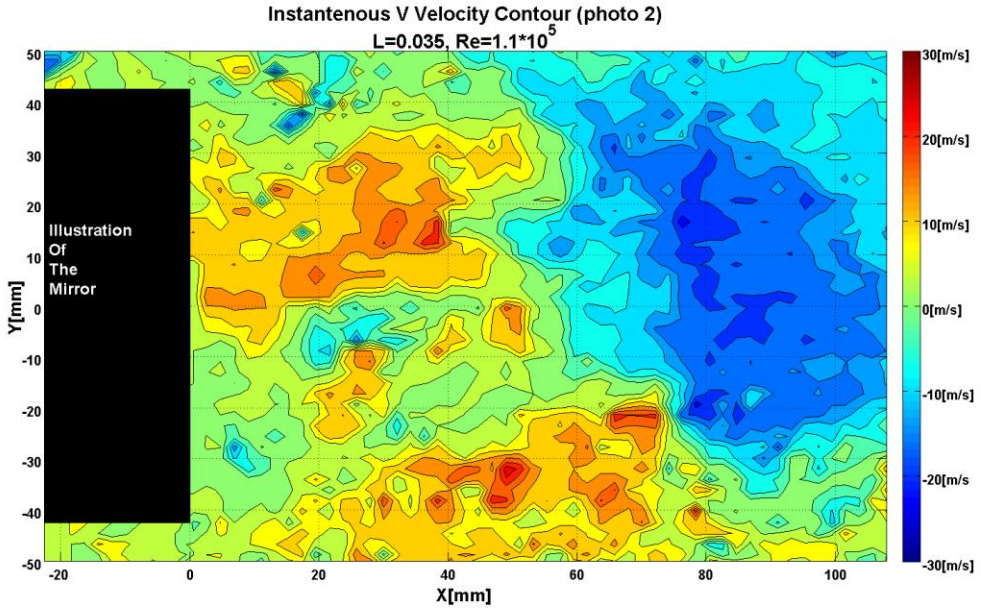

(b)

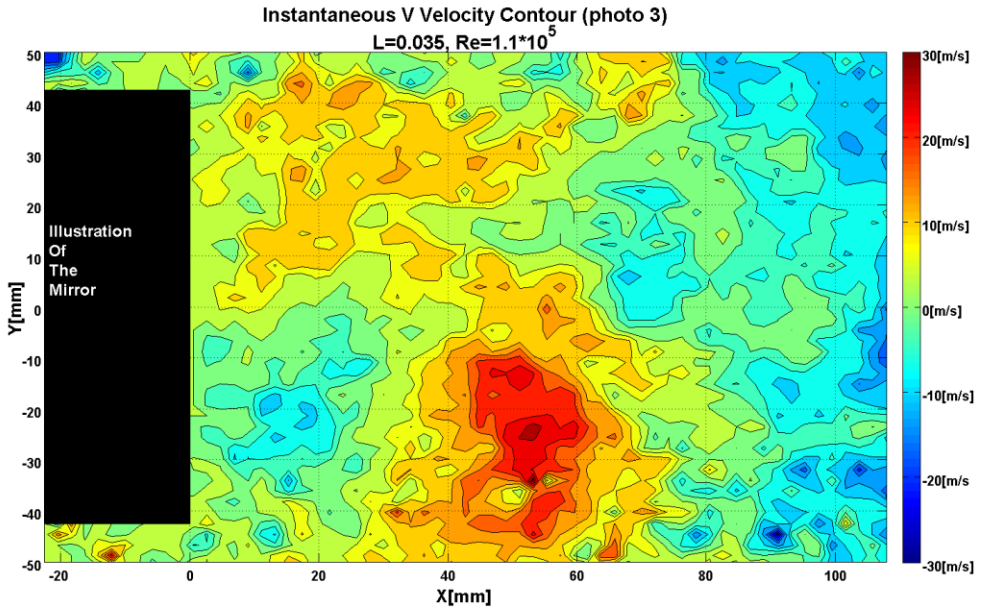

(c)

Figure 10 – PIV results for instantaneous velocity contours for flow field behind the mirror at subsequent time with a time interval of Δt=0.5 [sec].

3.3 The Drag and the Recirculation Length

Drag is measured using the wind tunnel's balance. For each drag measurement approximately one minute was waited for the system to stabilize. Afterwards two samples are taken and averaged. It was noticed that the two samples differ by less than 0.01% for all measurements. For each sample the fluid conditions were taken in order to calculate the Reynolds number and air density. For one mirror glass location, measurements start with low Reynolds number and the wind tunnel speed is gradually increased to obtain data for all six Reynolds numbers. At the end of each set of measurements the lowest Reynolds number was tested again for repeatability analysis. It was found that the Reynolds

number differs by less than 1.5% and that the measurements reported the same behaviour with a different in the results of 0.2%.

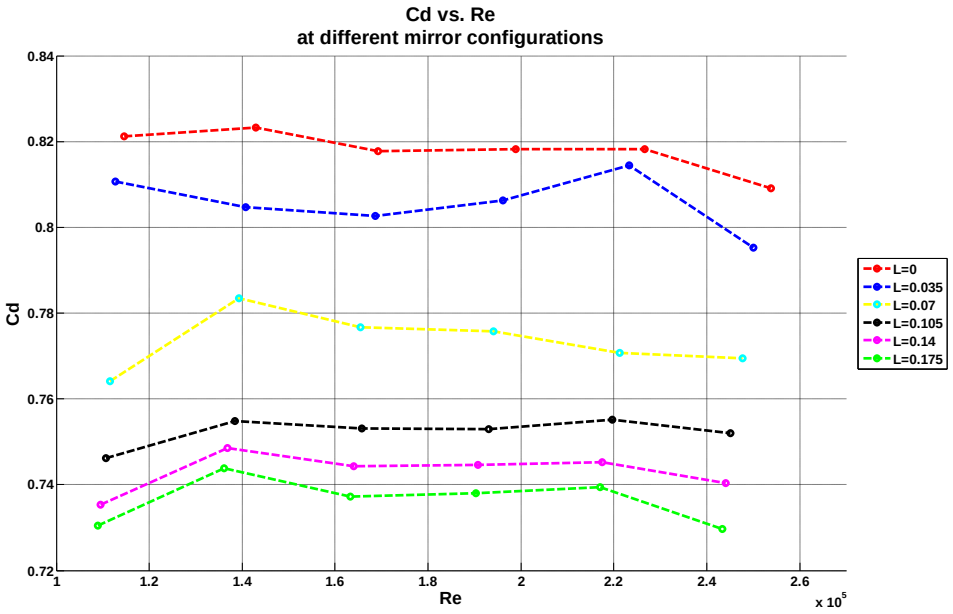

Figure 11 – Drag coefficient plotted against Re at different mirror's configurations

The experimental results for the drag coefficient are shown in Figure 11. It can be seen that as the glass is located further inside its frame, which corresponds to an increase in L, the drag coefficient decreases at all Reynolds numbers. The maximum drop is approximately 11% happened at $Re = 2.6 \times 10^5$ and $L = 0.175$, as can be seen in Figure 12. In addition, the drag coefficient does not change much for different Reynolds numbers up to $Re \cong 2.2 \times 10^5$ where a small drop is noticed.

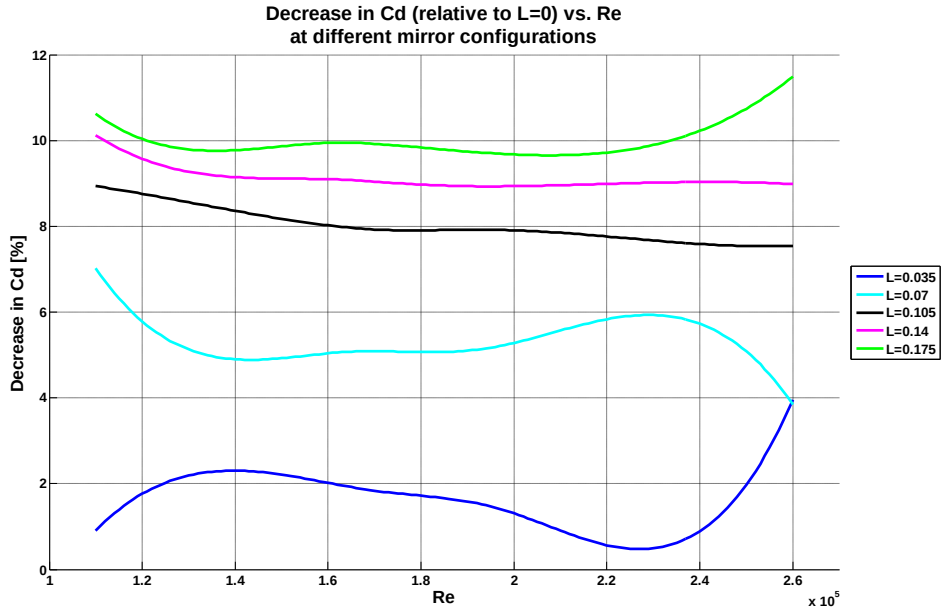

Figure 12 – Decrease in Cd (relative to L=0) plotted against Re for different mirror configurations

The recirculation length was extracted from the PIV mean velocity results (Contours of measured velocity are given in Figure 16-21 in Appendix A). The recirculation length is defined as the distance from

the centre of its glass to the point in the wake where the velocity in the *x* direction is zero. Two, absolute and effective, recirculation lengths have been calculated. The absolute value is defined as the distance relative to the mirror's centre and the relative is defined as the distance relative to the mirror's glass.

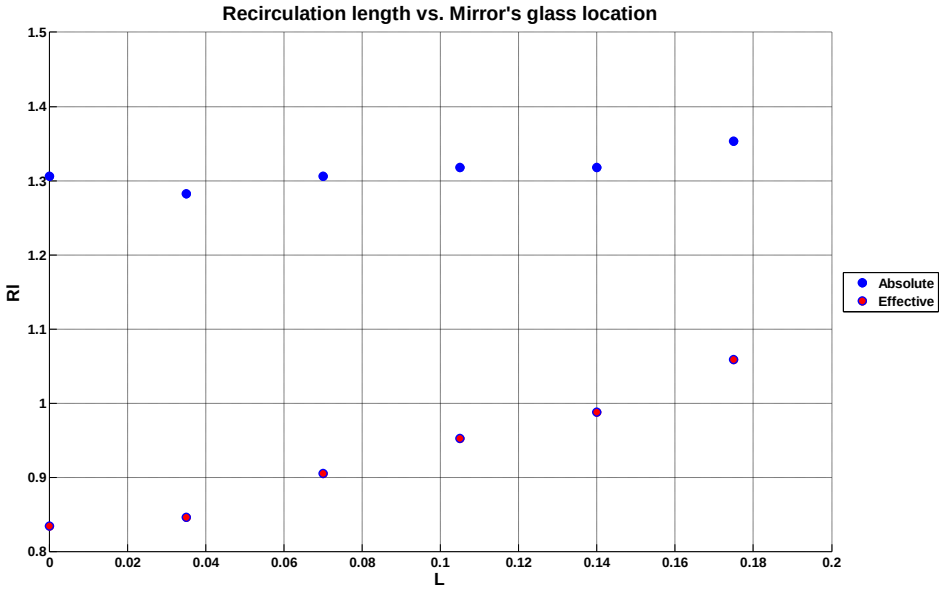

Figure 13 – Recirculation length vs. mirror's glass location

As can be seen in Figure 13, the recirculation lengths, both the absolute and the effective, are getting larger as the mirror's glass is placed further inside its frame. It should be mentioned that the reason for defining two different recirculation lengths was due to the CFD results which predicted opposing behaviour in the results of the two.

The results for the effective recirculation length support the Bearman and Trueman's observation [3] that the drag coefficient and the recirculation length are correlated, an increase in the recirculation length results in a decrease in the drag coefficient. They also noticed correlation to the back pressure but due to lack in back pressure measurement this couldn't be validated.

An intuitive explanation for the enlargement in the recirculation length is that the movement of the mirror's glass inside its frame sucks the recirculation flow further inside the cavity behind the mirror, but at the same time it doesn't sucks its downstream edge towards the mirror but even push it slightly away. The reason for this behaviour could be explained that the downstream edge is only affected by the outer shape of the mirror and is not affected by the location of the mirror. All this together cause an enlargement of the recirculation region which is correlated with a decrease in the drag coefficient as mentioned above. Further investigations are needed to explain the physics for this phenomenon.

3.4 Energy Spectra and Vortex Shedding Frequency

HWA was used to measure the energy spectra in a fixed point just outside the wake to investigate the mirror's vortex shedding characteristics, especially the shedding frequency. The results are plotted in Appendix B. A primary peak, which corresponds to the vortex shedding frequency, is observed in the energy spectra for each case. The peak frequency only varies with Reynolds number and stays constant when the glass position is changed. In addition, a small peak can also be noticed at higher frequency, as can be seen in Figure 14, which is the harmonic and doubles the fundamental frequency. This result is known for spheres in uniform flow at $200 < Re < 200000$ which again might indicate on similarity in the flow behaviour to spheres. For spheres, the lower frequency is attributed to the large-scale instability of the wake and is independent of the Reynolds number and its related Strouhal number is approximately equal to 0.2. The higher frequency Strouhal number is caused by small-scale instabilities

from the separation of the shear layer [7]. For the mirror case the Strouhal number for the fundamental frequency is relatively higher – approximately 0.26. This change in the Strouhal number is expected as the mirror has a shape of elongated half cylinder rather than a sphere. In addition, another similarity to a sphere is noticed that the Strouhal number is not changing with Reynolds number in the investigated regime, as can be seen in Figure 14.

In addition, this result indicates that the vortex shedding frequency is not influenced by the trailing edge shape of the mirror and has, in aeroelasticity meanings, no effect on the mirror's required structure properties.

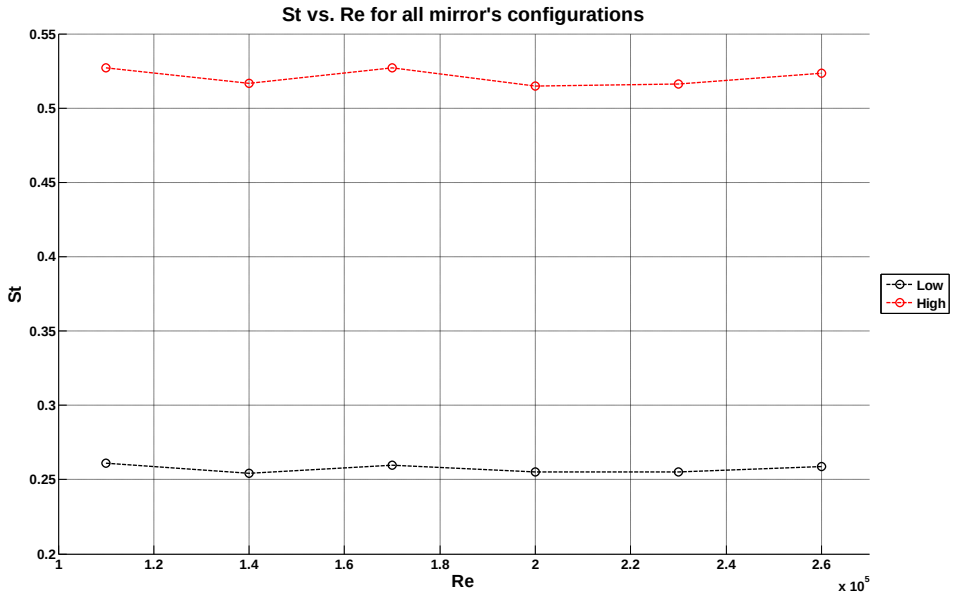

Figure 14 – Strouhal number plotted against Reynolds number for all mirror configurations.

3.5 Velocity Profile Downstream

Using a pitot-static tube the mean velocity profile of the wake was measured. The results, as can be seen in Figure 15, don't show any clear trend for different mirror glass location - the different wake profiles seem to be blending one with the other.

Two reasons could be appointed for that behaviour. First the velocity profile isn't changing enough with the change of the mirror's location inside its frame such that it can be captured by the Betz gate. Secondly, which seems more reasonable, the vibrations of the construction which was holding the Pitot - static tube due to the flow were too strong. Adding it to the change in the flow conditions (Reynolds number) during each measurement lead to a large enough uncertainty in the results such that clear results could not be achieved (as have been discussed in 2.3.6).

In general, a velocity profile of a wake is such that the velocity at the centre of the wake is lower than at its borders. It can be clearly noticed that even though the results obtained seem to have been influenced by measurement conditions a general wake profile is obtained. In addition, it can be seen that the decrease in the velocity at the centre of the wake is approximately22%. Also, the wake width is very large at that point (larger than the measured range of 4.5 times the mirror diameter). This indicates that any aerodynamic feature behind the mirror, for example the rear wing, will be affected by the mirror's wake.

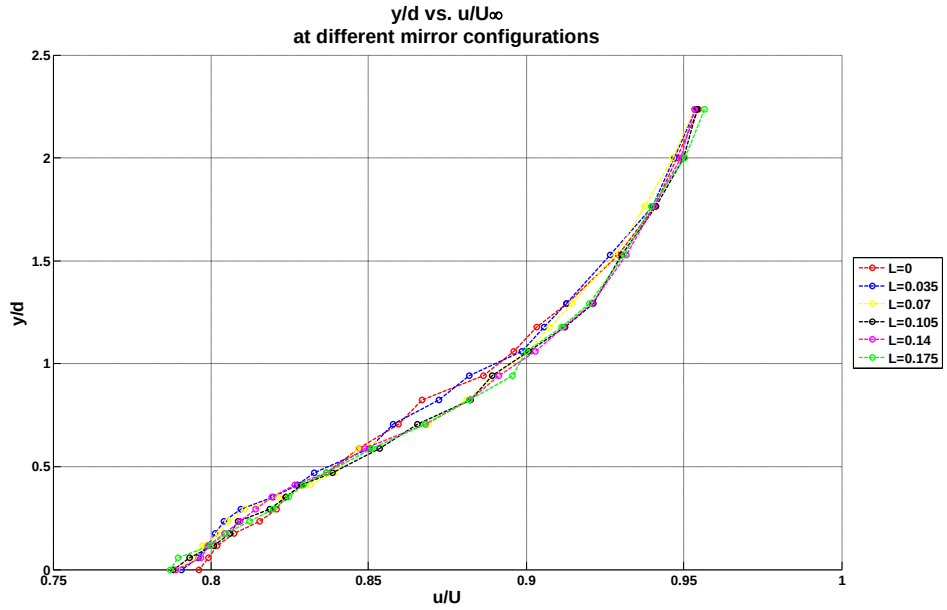

Figure 15 - Velocity profile in the wake, h/d=14.1 downstream

3.6 Some Computational Results

The computational results have been obtained for 2D RANS using the commercial solver Fluent. Different turbulent models have been tested, none of the models except the Spalart-Allmaras model converges to physically correct solution. In addition, large differences have been noticed between the computational and the experimental results.

The trend of changes in the drag coefficient after moving the mirror glass is different for the computational and the experimental results. While the experimental results show decrease in the drag coefficient of 10-11% the computational results show almost no change – 0.01% increase. In addition, the drag coefficient predicted computationally is lower by up to 85% compared to the experimental data. Moreover, the behaviour of the recirculation length is also different. While in the experimental results both the effective and the absolute recirculation lengths are getting larger as the mirror's glass is located further inside its frame the computational results show an increase for the effective one and a decrease for the absolute for the same change. In addition, the predicted recirculation length by the computational approach is higher by up to 85% than the experimental results. This result was expected due to the much lower drag coefficient predicted by the computational approach and the known correlation between the drag coefficient and the recirculation length.

Regarding to the wakes profile, no full comparison could be made due to the fact that the experimental results contain a very large uncertainty. On the other hand a quantitative comparison was made and found that the computational approach was estimating a faster velocity in the wake by up to 10%. The increase in the velocity could be coming from the blockage effect (conservation of mass) but the domain study that was done shows that this shouldn't be the case. Such, that error could be coming from the general error in the computational approach.

In conclusion, the computational RANS approach failed to predict correctly any changes in the RVSM's performance in compare to the experimental approach.

4. Conclusions and Proposed Future Work

The aerodynamic performance of F1 RVSM is investigated for the effect of its glass location inside the frame. Two different approaches of investigation have been used - computational, using the commercial solver Fluent and the Spalart-Allmaras turbulent model, and experimental, using the University of Southampton $7' \times 5'$ wind tunnel and a specially designed 2-D model. The flow was investigated at six different positions of the mirror's glass. Here is a summary of the main conclusions:

- The mirror's drag decreases by 10%-11% when the glass is located further inside its frame for all investigated Reynolds numbers. This change corresponds to a 0.5% decrease in drag for a road car where RVSM is estimated to contribute 5% of the car's drag.
- No noticeable change has been found in the vortex shedding frequency for different configurations. This means that the change of mirror glass location has no effect on the vortex shedding frequency. In addition, this means that this modification has neither structure advantage nor disadvantage.
- The recirculation length increases with the glass positioned further inside its frame due to the "suction" that was created inside the mirror's frame.
- Similarity of the wake structure to the upper sub-critical and critical regimes of a circular cylinder was noticed based on the drag coefficient behaviour, the Strouhal number behaviour and flow structure of the wake.
- The computational RANS approach failed to predict correctly the flowfield around the mirror and in addition failed to predict any flow changes due to the different configurations based on experimental evidence.

The achieved results indicate that the tested modification is correlated to a decrease in the mirror's drag. This advantage has a great meaning in the F1 industry but also in the automotive engineering industry. Due to that fact the following proposed studies should be done:

- Since the tested model was a two-dimensional mirror, and based on previous studies (See 1.2) the flow around a RVSM is fully three-dimensional, a three-dimensional model should also be tested.
- Since the computational RANS approach has failed more accurate computational approaches, like DES and LES, should be considered in future research.
- Since the flow around the mirror is affected by the car's body a future study should be done on a small scale F1 car model in order to investigate whether this advantage is also gained on the car as a whole and not just on the mirror as an individual component.

5. Acknowledgments

We would like to acknowledge Dr Gary N Coleman for his willingness to take forward the proposed inventive research. In addition, we would like to acknowledge Takafumi Nishino for long hours of discussion and for his help at the wind tunnel with the PIV system. Also, we would like to acknowledge Mike Tudorpole for his great help in the wind tunnel during the experiments' period and for his constant support during the design of the wind tunnel model.

6. Bibliography

[1] Achenbach, E., Influence of Surface Roughness on the Cross-Flow around a Circular Cylinder, *Journal of Fluid Mechanics*, Vol. 46, pp. 321-335, 1971.

[2] Baker, C.J., The Turbulent Horseshoe Vortex, *Journal of Wind Engineering and Industrial Aerodynamics,* Vol. 6, pp. 9-23, 1980.

[3] Bearman, P.W. and Trueman, D.M., An Investigation of the Flow around Rectangular Cylinders, *Aeronautical Quarterly*, 229-237, 1972.

[4] Bearman, P.W., On the Vortex Shedding from a Circular Cylinder in the Critical Reynolds Number Regime, *Journal of Fluid Mechanics*, Vol. 37, pp. 577-585, 1969.

[5] G. Bosch and W. Rodi, Simulation of Vortex Shedding Past a Square Cylinder With Different Turbulence Models, *International Journal For Numerical Methods in Fluids*, Vol. 28, pp. 601-616, 1998.

[6] Joel H. Ferziger, and Milovan Petric, *Computational Methods for Fluid Dynamics*, 3rd Edition, Springer, 2002.

[7] Kim K. J. and Durbin P. A., Observations of the frequencies in a sphere wake and drag increase by acoustic excitation, Journal of *Physics of Fluids*, 31, pp. 3260-3265, 1988.

[8] Milne-Thomson L.M., *Theoretical Hydrodynamic*, MACMILLAN Press, New York, 1968.

[9] Morkovin, M.V., Flow around a Circular Cylinder - A Kaleidoscope of Challenging Fluid Phenomena, Symposium on Fully Separated Flows, ed. A.G. Hansen, *American Society of Mechanical Engineers*, pp. 102-118, 1964.

[10] Roshko, A., Experiments on the Flow Past a Circular Cylinder at Very High Reynolds Number, *Journal of Fluid Mechanics*, Vol. 10, pp. 345-356, 1961.

[11] S. Szepessy, P. W. Brearman, Aspect Ratio and End Plate Effects on Vortex Shedding from a Circular Cylinder, *Journal of Fluid Mechanics*, Vol. 234, pp. 191-217, 1992.

[12] Schlichting, H., *Boundary Layer Theory*, 7th Edition, McGraw-Hill, New York, 1979.

[13] Simon Watkins and Greg Oswald, The Flow Field of Automobile Add-ons — With Particular Reference to the Vibration of External Mirrors, *Journal of Wind Engineering and Industrial Aerodynamics*, Vol. 82, pp. 541-554, 1999.

[14] Surry D., Some Effects of Intense Turbulence on the Aerodynamics of a Circular Cylinder at Sub-Critical Reynolds number, *Journal of Fluid Mechanics*, Vol. 52, pp. 543-563, 1972.

[15] Takafumi Nishino, An Investigation of Flow Around a Circular Cylinder in Ground Effect, PhD Transfer Thesis, 2006.

[16] University of Southampton Wind tunnels' website: http://www.windtunnel.soton.ac.uk/

[17] Wolf-Hienrich Hucho, *Aerodynamics of Road Vehicles*, 4th Edition, 1998.

[18] Zdravkovich, M. M., Conceptual Overview of Laminar and Turbulent Flows Past Smooth and Rough circular cylinders, *Journal of Wind Engineering and Industrial Aerodynamics*, Vol. 33, pp. 53-62, 1990.

[19] Zdravkovich, M.M., *Flow around Circular Cylinders: Volume 1: Fundamentals*, Oxford University Press, Oxford, UK, 1997.

[20] Zdravkovich, M.M., *Flow around Circular Cylinders: Volume 2: Applications*, Oxford University Press, Oxford, UK, 2003.

Appendix A PIV Results - Figures

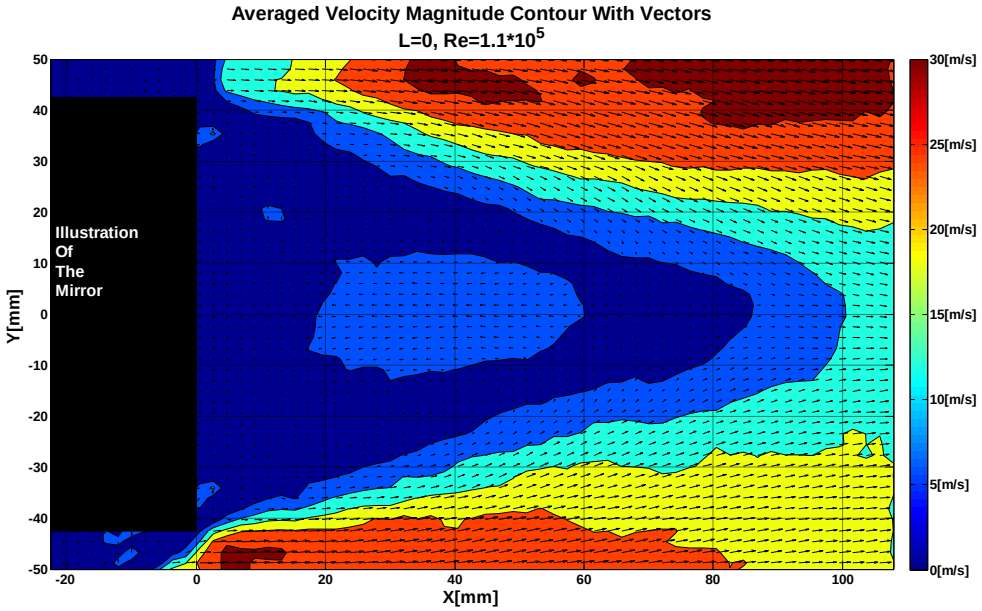

Figure 16 - Averaged Velocity Magnitude Contour Including Vectors, L=0, Re=1.1x10^5.

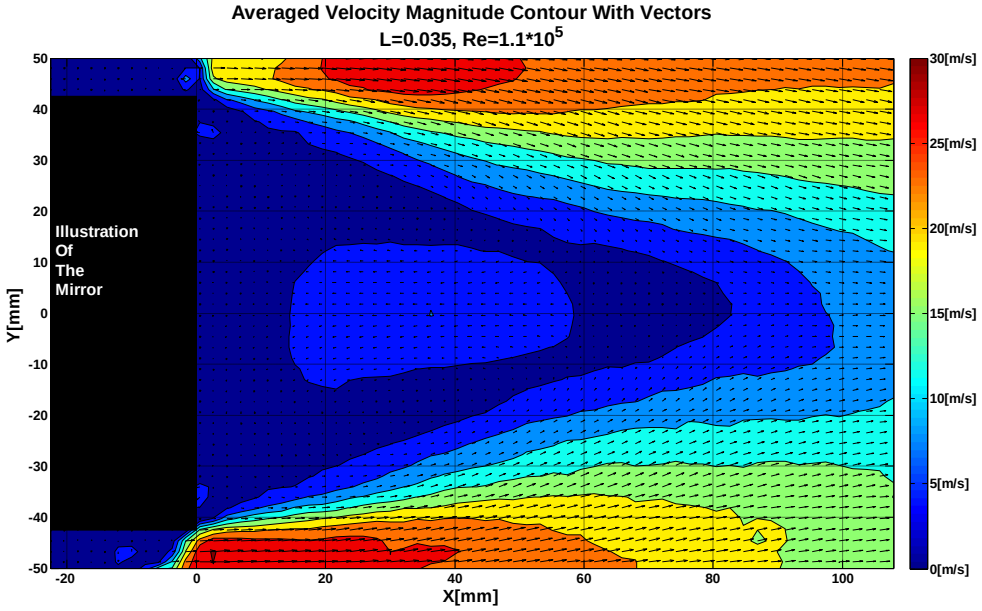

Figure 17 - Averaged Velocity Magnitude Contour Including Vectors, L=0.035, Re=1.1x10^5.

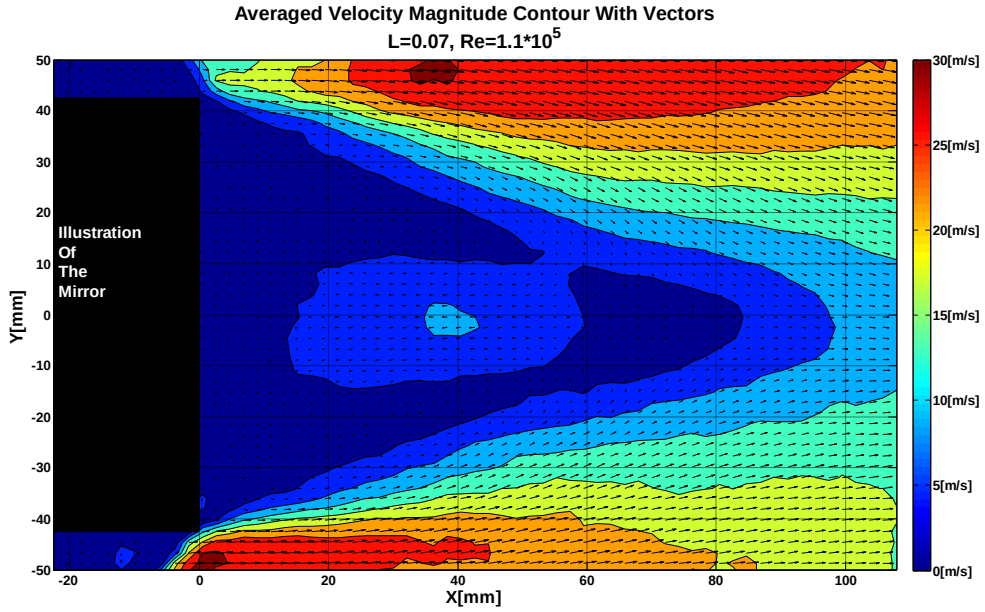

Figure 18 - Averaged Velocity Magnitude Contour Including Vectors, L=0.07, Re=1.1x10^5.

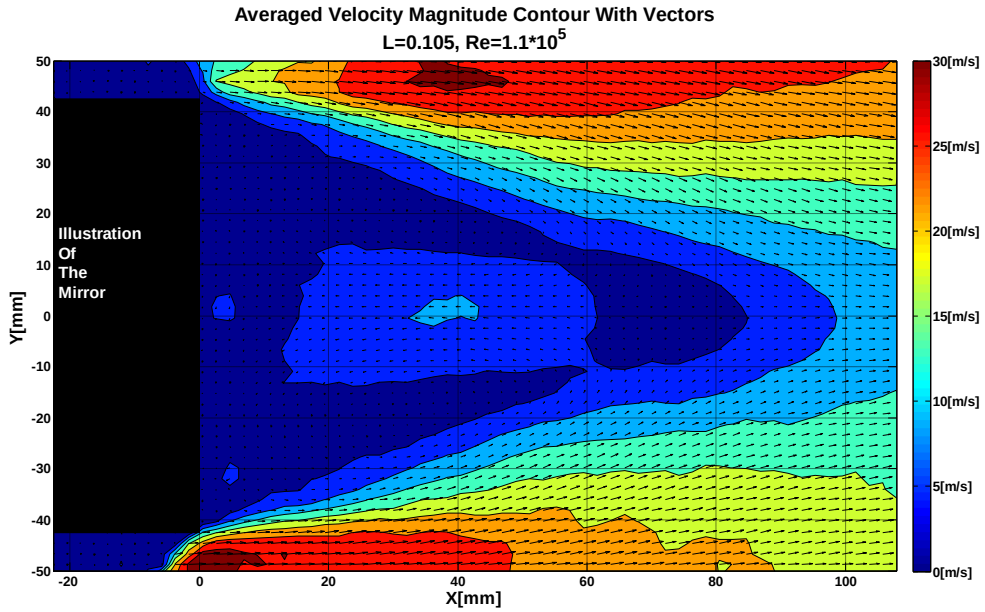

Figure 19 - Averaged Velocity Magnitude Contour Including Vectors, L=0.105, Re=1.1x10^5.

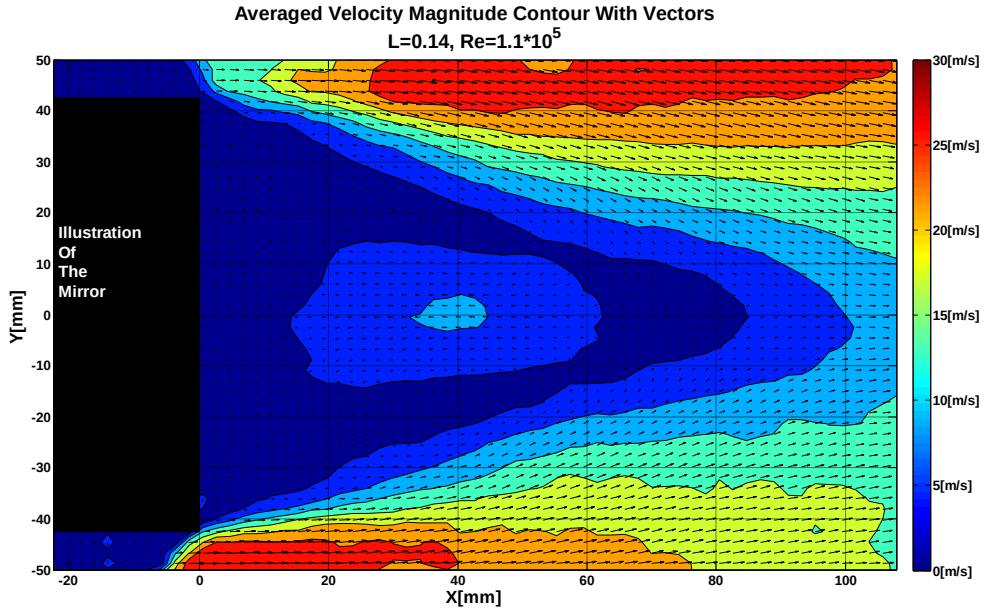

Figure 20 - Averaged Velocity Magnitude Contour Including Vectors, L=0.14, Re=1.1x10^5.

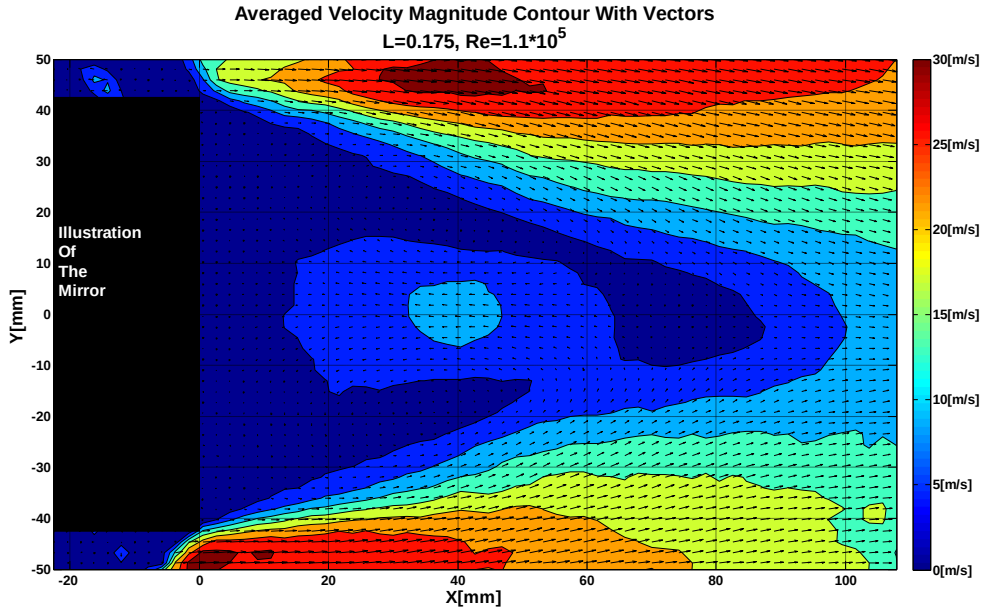

Figure 21 - Averaged Velocity Magnitude Contour Including Vectors, L=0.175, Re=1.1x10^5.

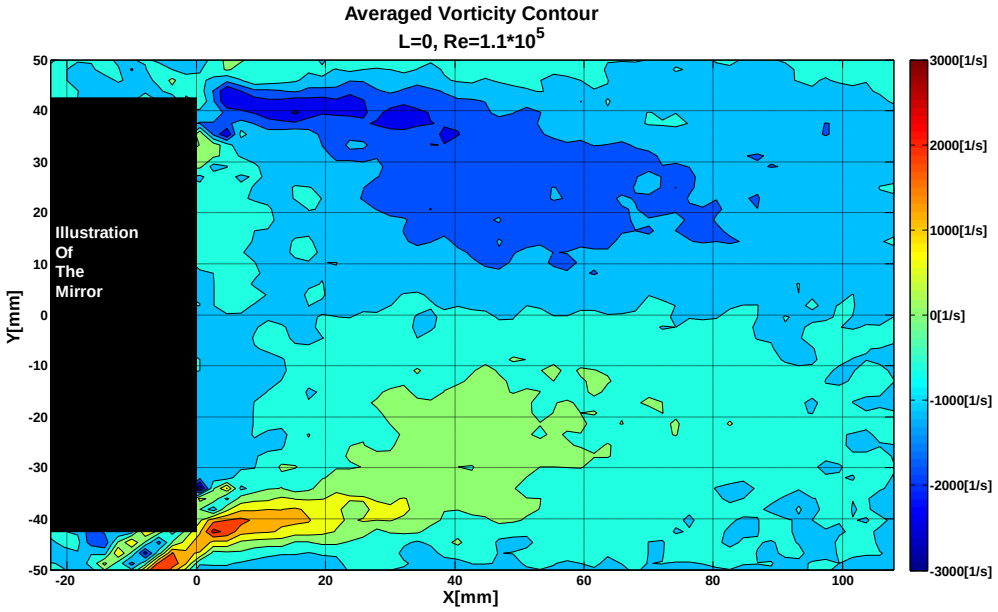

Figure 22 - Averaged Vorticity Contour, L=0, Re=1.1x10^5.

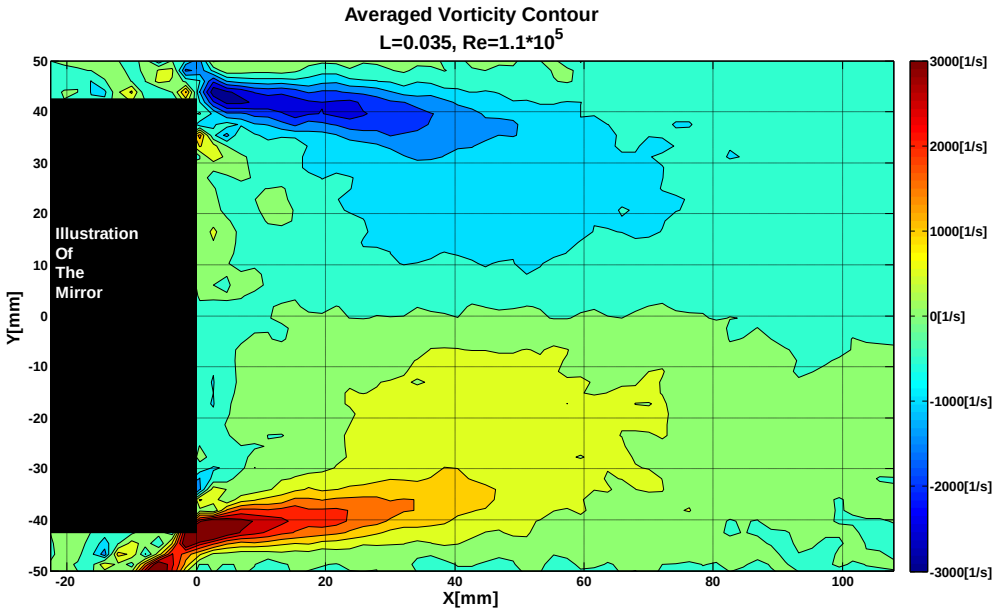

Figure 23 - Averaged Vorticity Contour, L=0.035, Re=1.1x10^5.

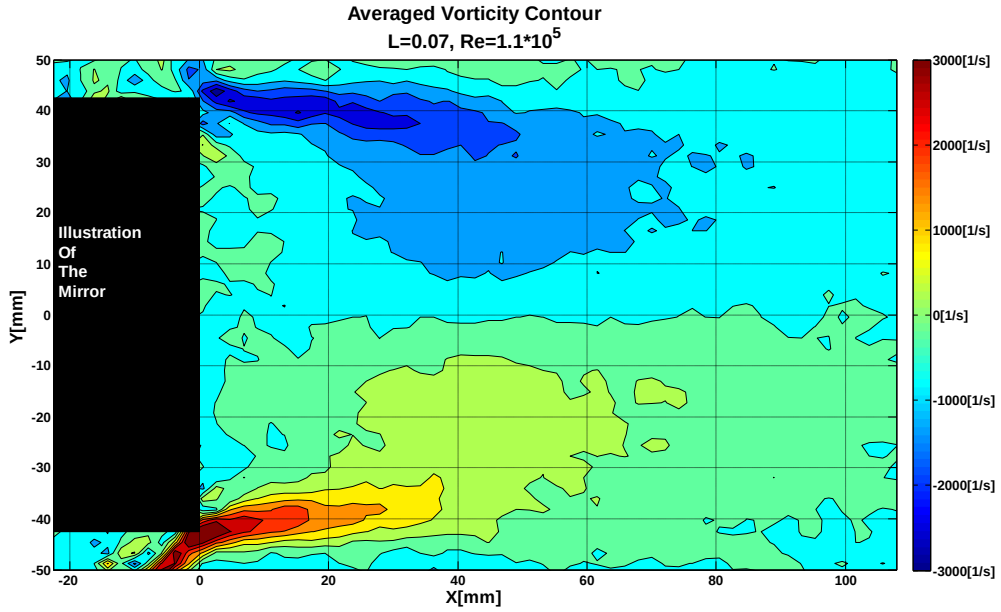

Figure 24 - Averaged Vorticity Contour, L=0.07, Re=1.1x10^5.

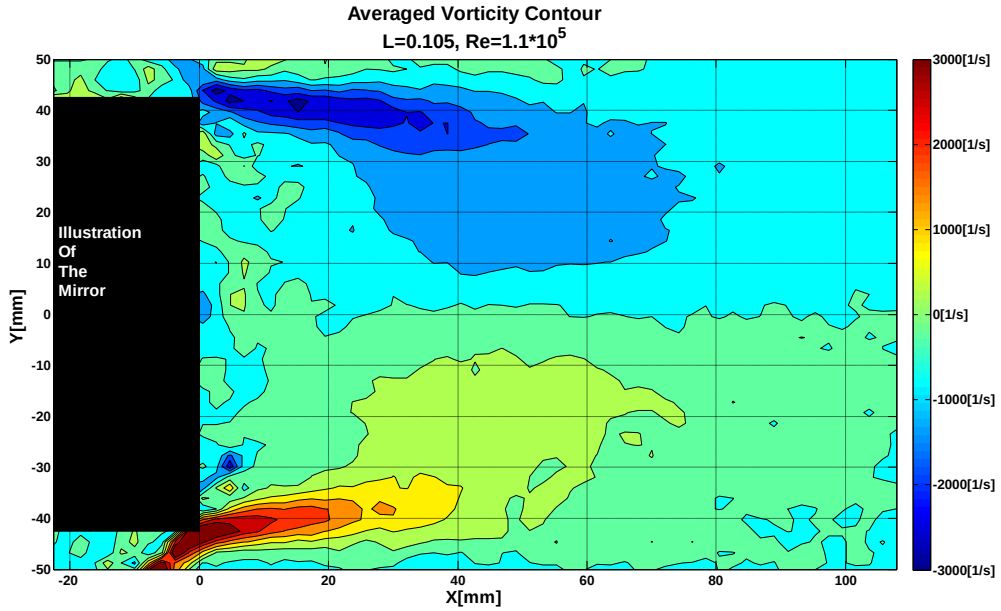

Figure 25 - Averaged Vorticity Contour, L=0.105, Re=1.1x10^5.

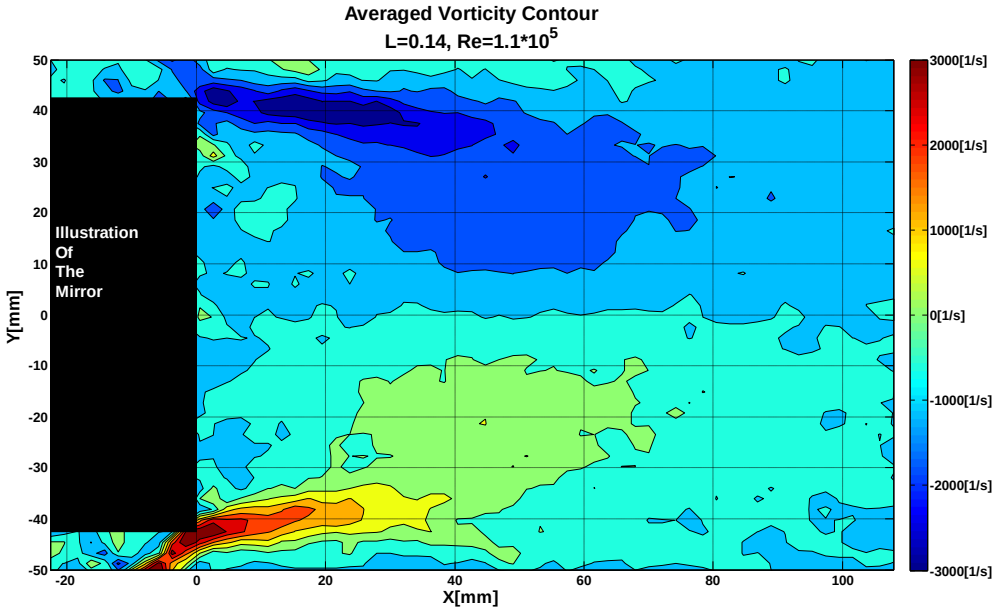

Figure 26 - Averaged Vorticity Contour, L=0.14, Re=1.1x10^5.

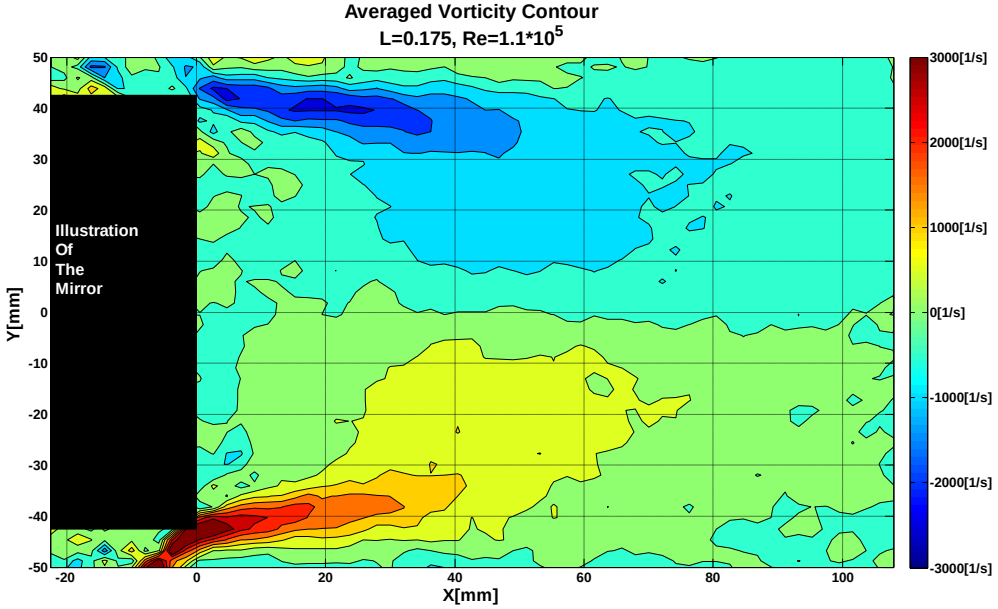

Figure 27 - Averaged Vorticity Contour, L=0.175, Re=1.1x10^5.

Appendix B HWA Results - Figures

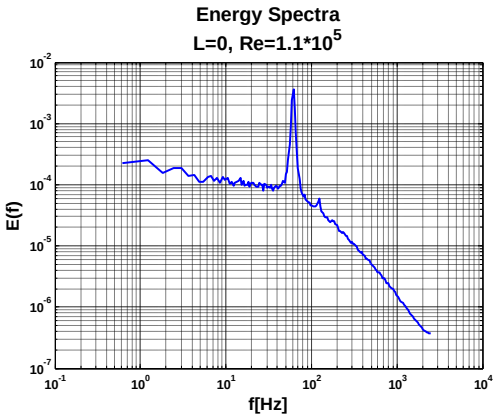

Figure 28 – Energy Spectra, L=0, Re=1.1x10^5.

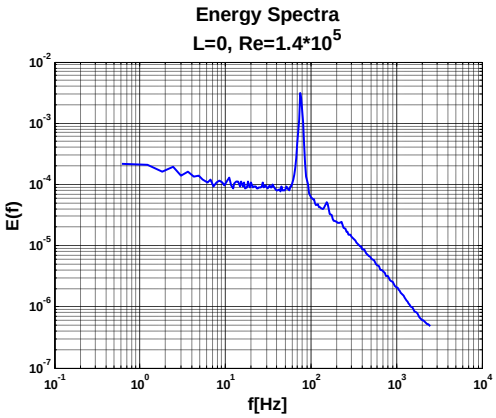

Figure 29 – Energy Spectra, L=0, Re=1.4x10^5.

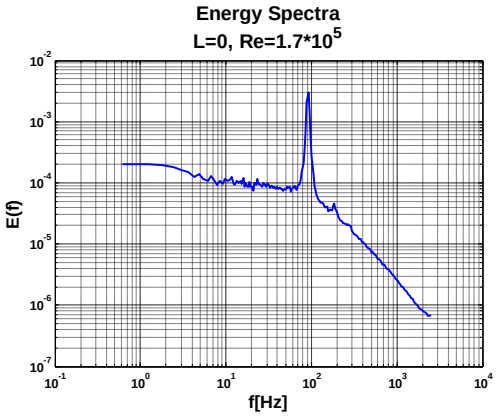

Figure 30 – Energy Spectra, L=0, Re=1.7x10^5.

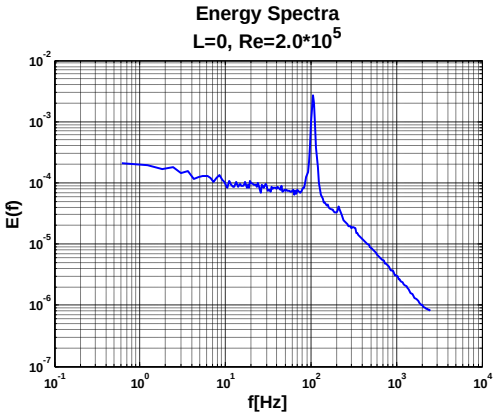

Figure 31 – Energy Spectra, L=0, Re=2.0x10^5.

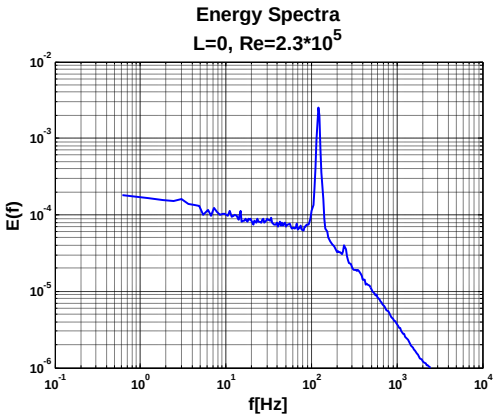

Figure 32 – Energy Spectra, L=0, Re=2.3x10^5.

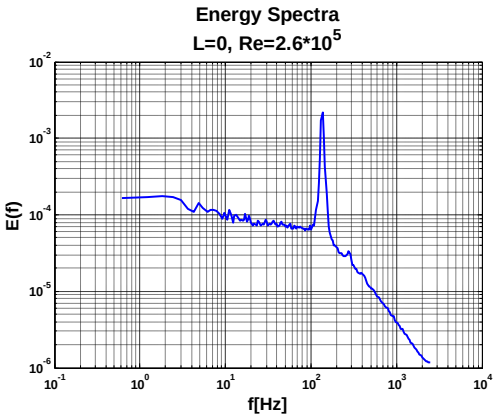

Figure 33 – Energy Spectra, L=0, Re=2.6x10^5.

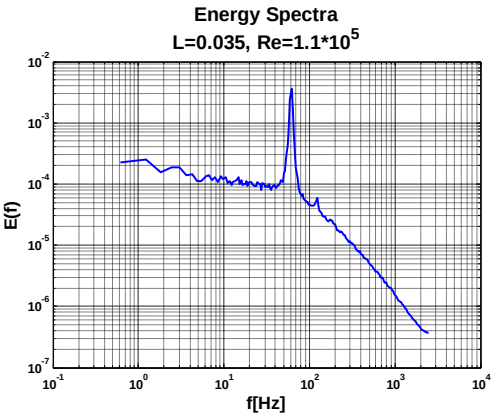

Figure 34 – Energy Spectra, L=0.035, Re=1.1x10^5.

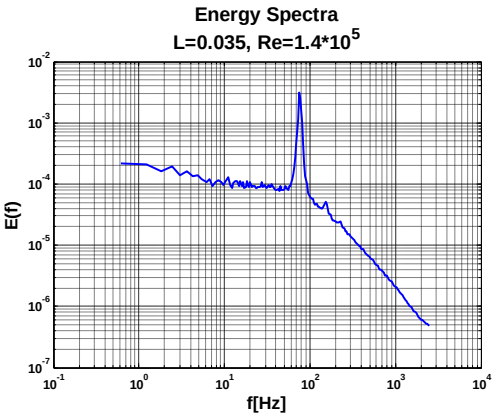

Figure 35 – Energy Spectra, L=0.035, Re=1.4x10^5.

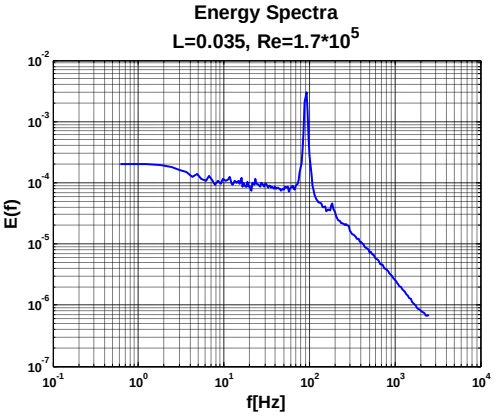

Figure 36 – Energy Spectra, L=0.035, Re=1.7x10^5.

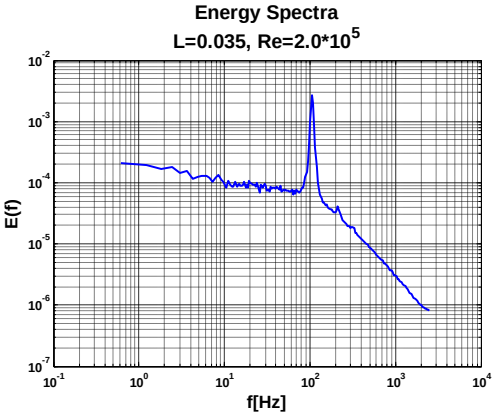

Figure 37 – Energy Spectra, L=0.035, Re=2.0x10^5.

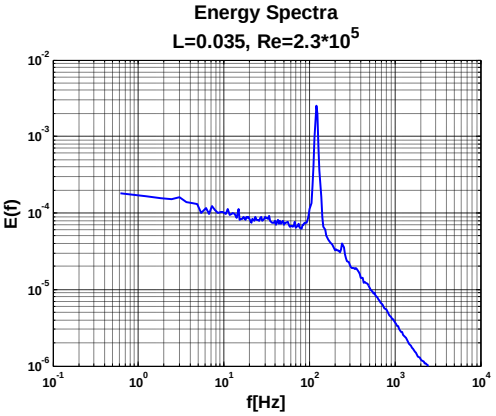

Figure 38 – Energy Spectra, L=0.035, Re=2.3x10^5.

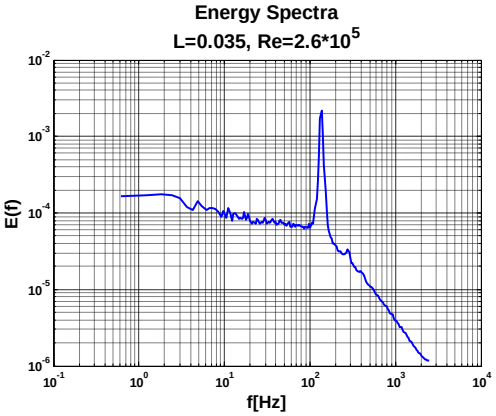

Figure 39 – Energy Spectra, L=0.035, Re=2.6x10^5.

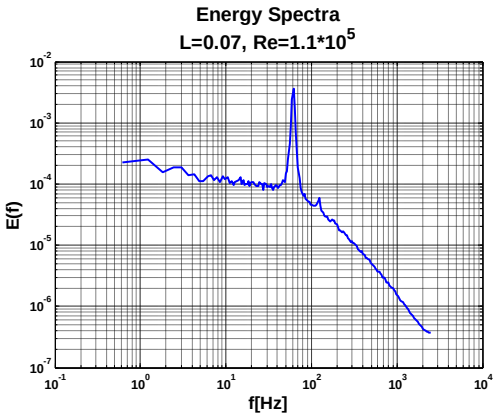

Figure 40 – Energy Spectra, L=0.07, Re=1.1x10^5.

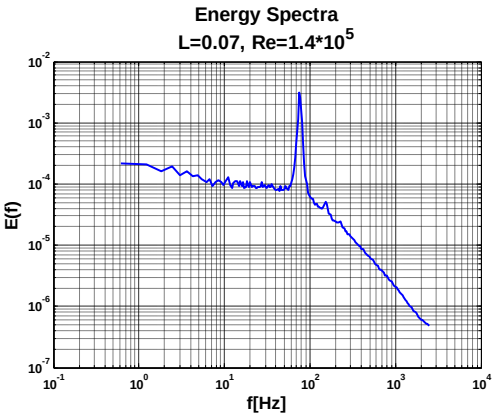

Figure 41 – Energy Spectra, L=0.07, Re=1.4x10^5.

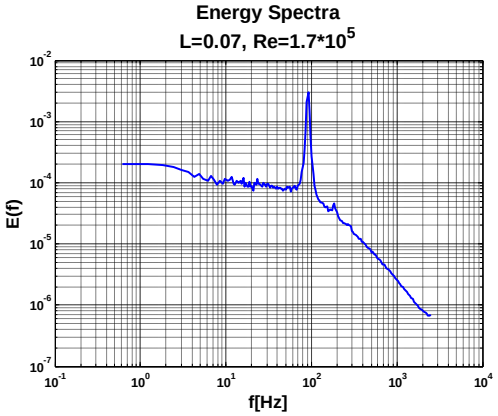

Figure 42 – Energy Spectra, L=0.07, Re=1.7x10^5.

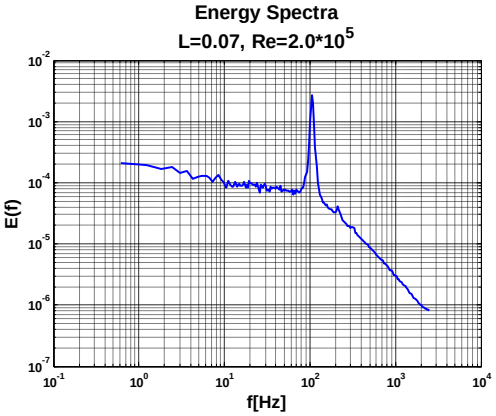

Figure 43 – Energy Spectra, L=0.07, Re=2.0x10^5.

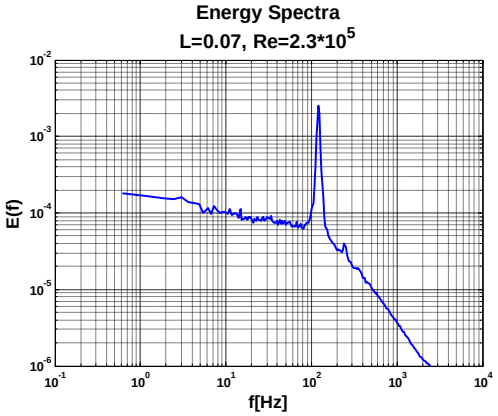

Figure 44 – Energy Spectra, L=0.07, Re=2.3x10^5.

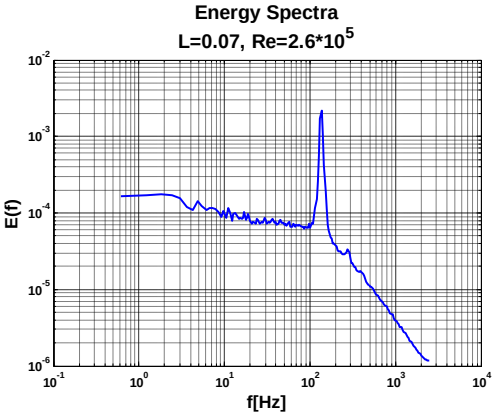

Figure 45 – Energy Spectra, L=0.07, Re=2.6x10^5.

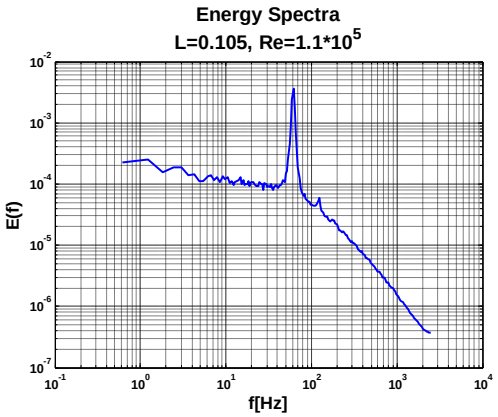

Figure 46 – Energy Spectra, L=0.105, Re=1.1x10^5.

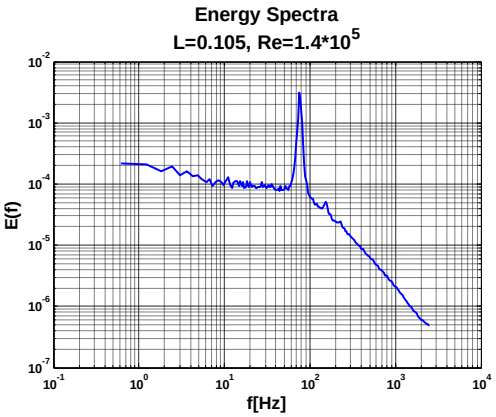

Figure 47 – Energy Spectra, L=0.105, Re=1.4x10^5.

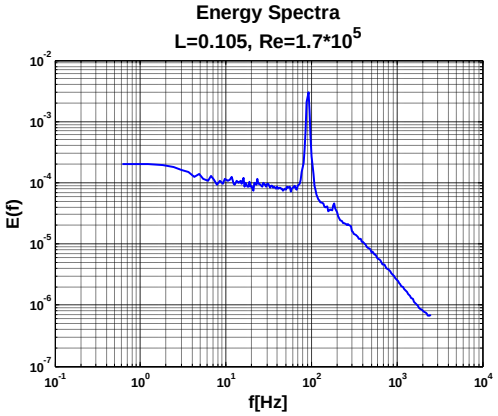

Figure 48 – Energy Spectra, L=0.105, Re=1.7x10^5.

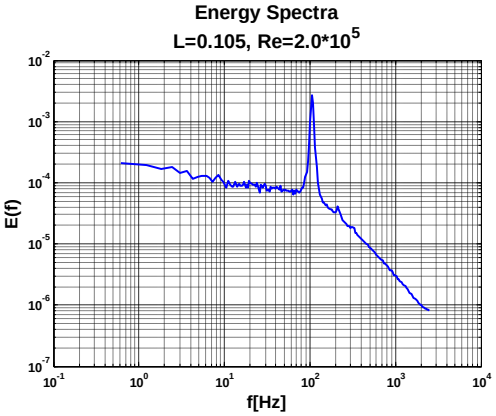

Figure 49 – Energy Spectra, L=0.105, Re=2.0x10^5.

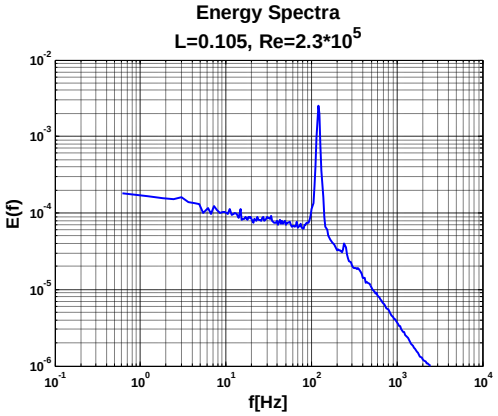

Figure 50 – Energy Spectra, L=0.105, Re=2.3x10^5.

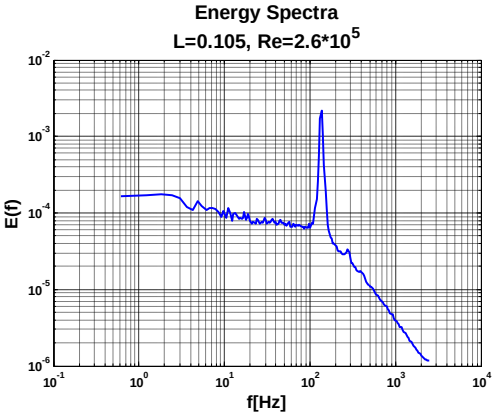

Figure 51 – Energy Spectra, L=0.105, Re=2.6x10^5.

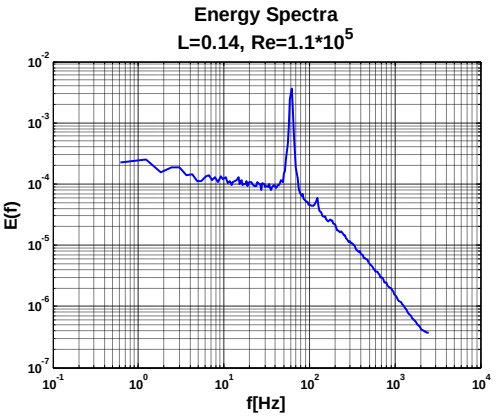

Figure 52 – Energy Spectra, L=0.14, Re=1.1x10^5.

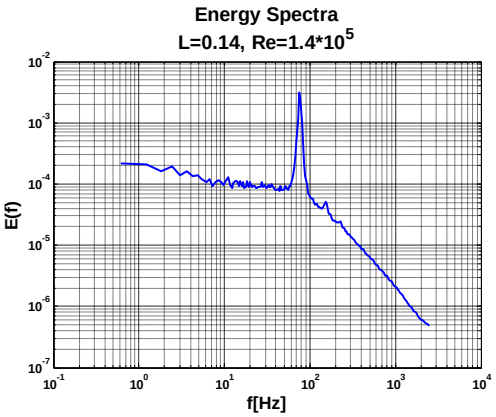

Figure 53 – Energy Spectra, L=0.14, Re=1.4x10^5.

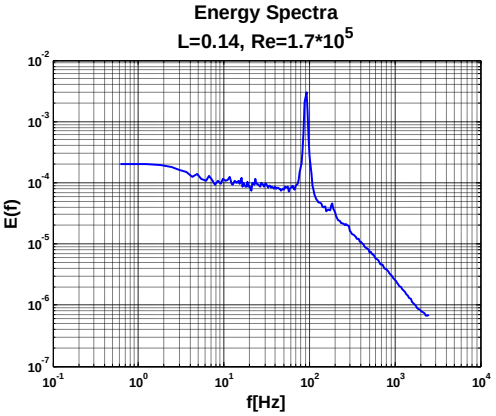

Figure 54 – Energy Spectra, L=0.14, Re=1.7x10^5.

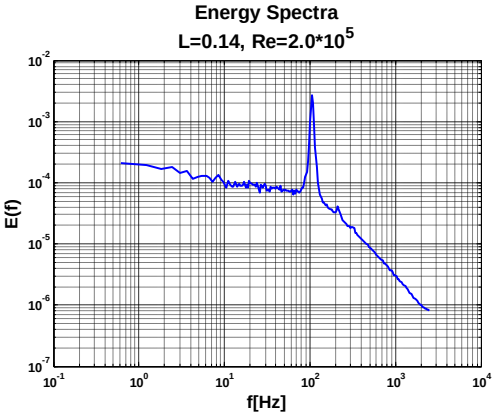

Figure 55 – Energy Spectra, L=0.14, Re=2.0x10^5.

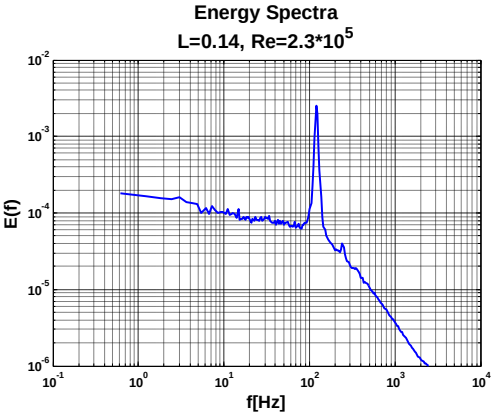

Figure 56 – Energy Spectra, L=0.14, Re=2.3x10^5.

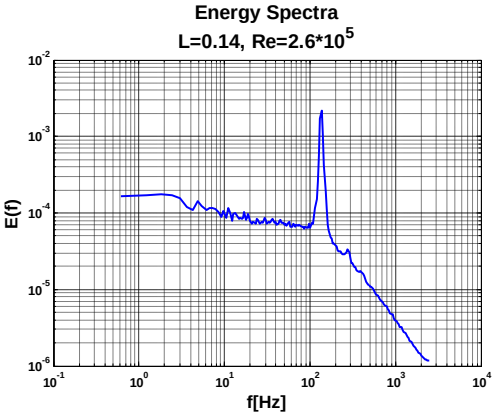

Figure 57 – Energy Spectra, L=0.14, Re=2.6x10^5.

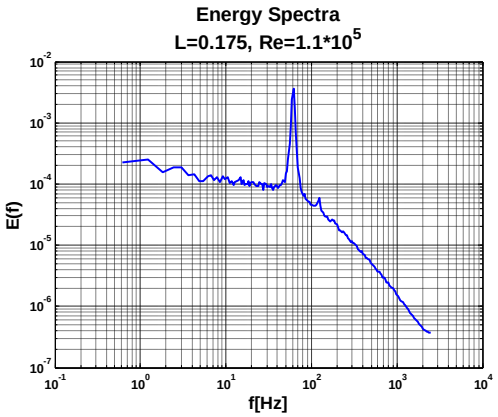

Figure 58 – Energy Spectra, L=0.175, Re=1.1x10^5.

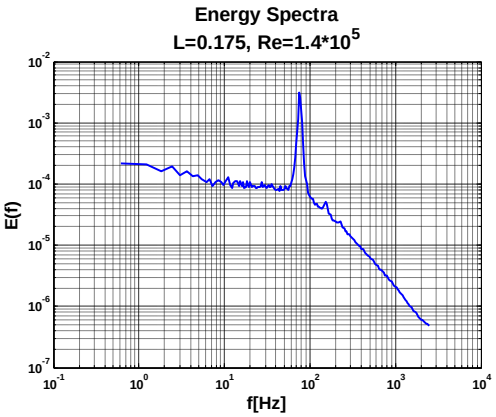

Figure 59 – Energy Spectra, L=0.175, Re=1.4x10^5.

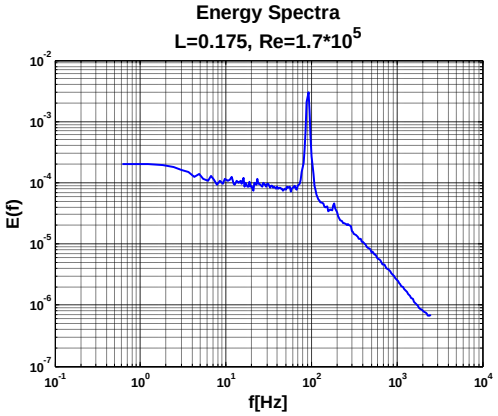

Figure 60 – Energy Spectra, L=0.175, Re=1.7x10^5.

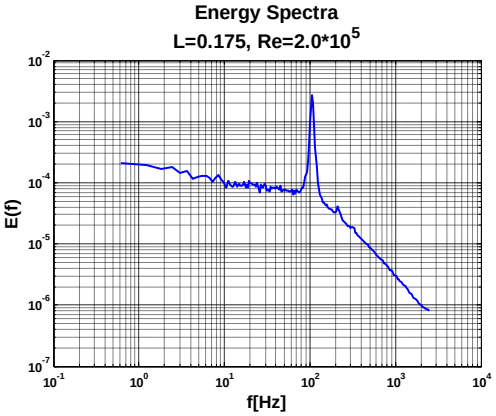

Figure 61 – Energy Spectra, L=0.175, Re=2.0x10^5.

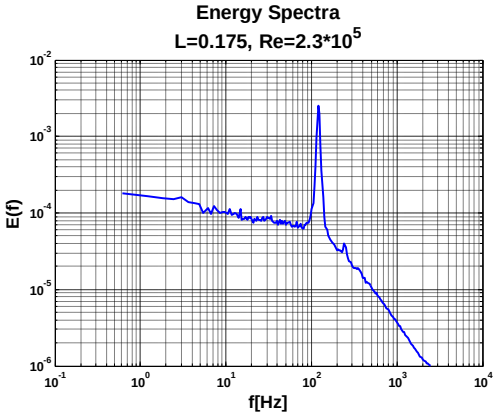

Figure 62 – Energy Spectra, L=0.175, Re=2.3x10^5.

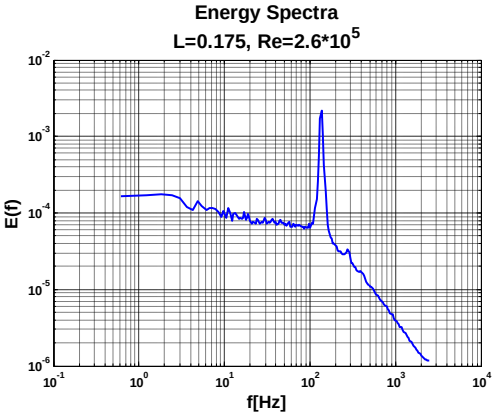

Figure 63 – Energy Spectra, L=0.175, Re=2.6x10^5.

Appendix C CAD Drawings

The following CAD drawings were created using the commercial CAD package Solid Edge.

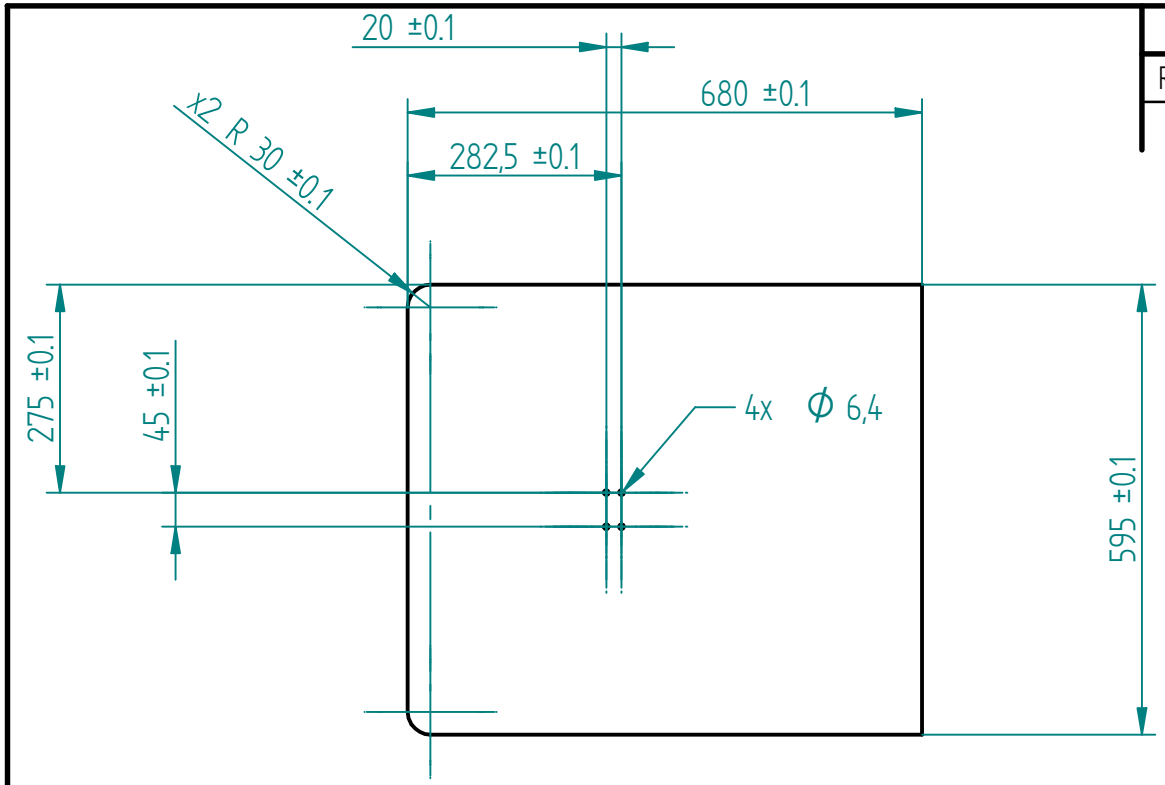

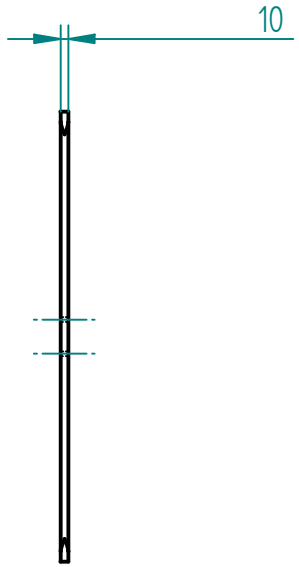

REVISION HISTORY			
REV	DESCRIPTION	DATE	APPROVED

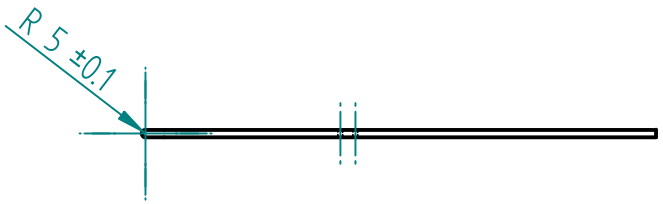

Material – Cast Clear Acrylic
Number of Parts –2
Texture – Clean

	NAME	DATE
DRAWN	Elad Rind	06/11/07
CHECKED		
ENG APPR		
MGR APPR		

UNLESS OTHERWISE SPECIFIED
DIMENSIONS ARE IN MILLIMETERS
ANGLES ±X.X°
2 PL ±X.XX 3 PL ±X.XXX

SOLID EDGE
UGS - The PLM Company

TITLE

SIZE	DWG NO	REV
A4		

FILE NAME: Draft.dft

SCALE: 1:10	WEIGHT:	SHEET 1 OF 18

REVISION HISTORY			
REV	DESCRIPTION	DATE	APPROVED

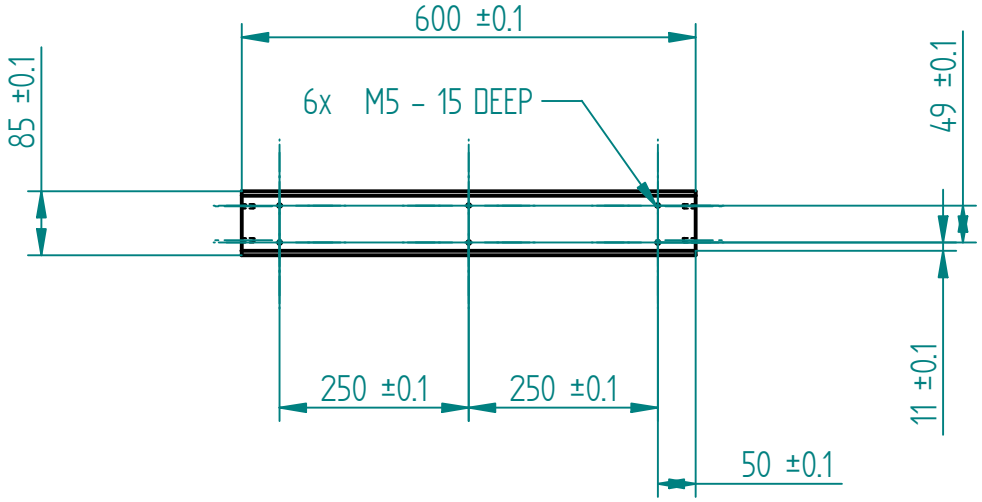

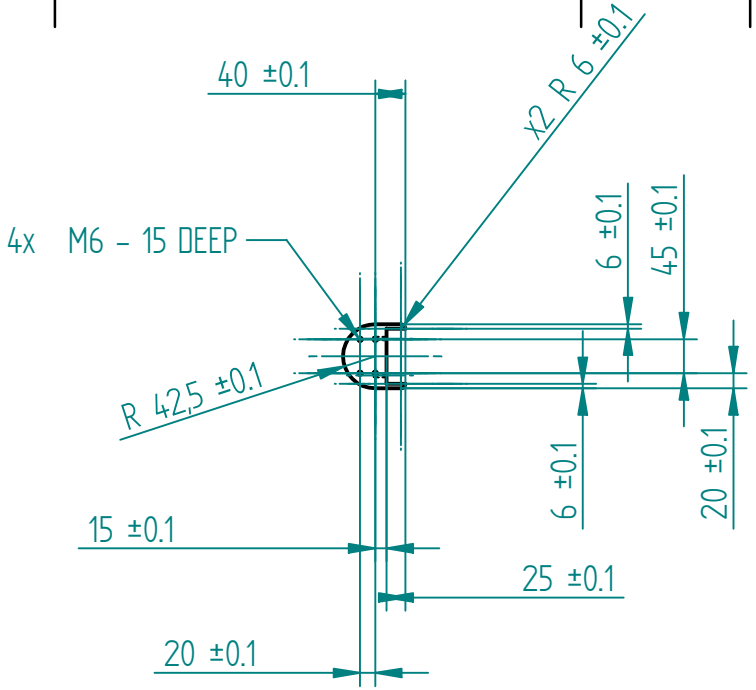

Material - Cibatool BM5440
Number of Parts - 1
Texture - Matt Black

	NAME	DATE
DRAWN	Elad Rind	06/11/07
CHECKED		
ENG APPR		
MGR APPR		

UNLESS OTHERWISE SPECIFIED
DIMENSIONS ARE IN MILLIMETERS
ANGLES ±X.X°
2 PL ±X.XX 3 PL ±X.XXX

SOLID EDGE
UGS - The PLM Company

TITLE

SIZE	DWG NO	REV
A4		

FILE NAME: Draft.dft

SCALE:1:10	WEIGHT:	SHEET 2 OF 18

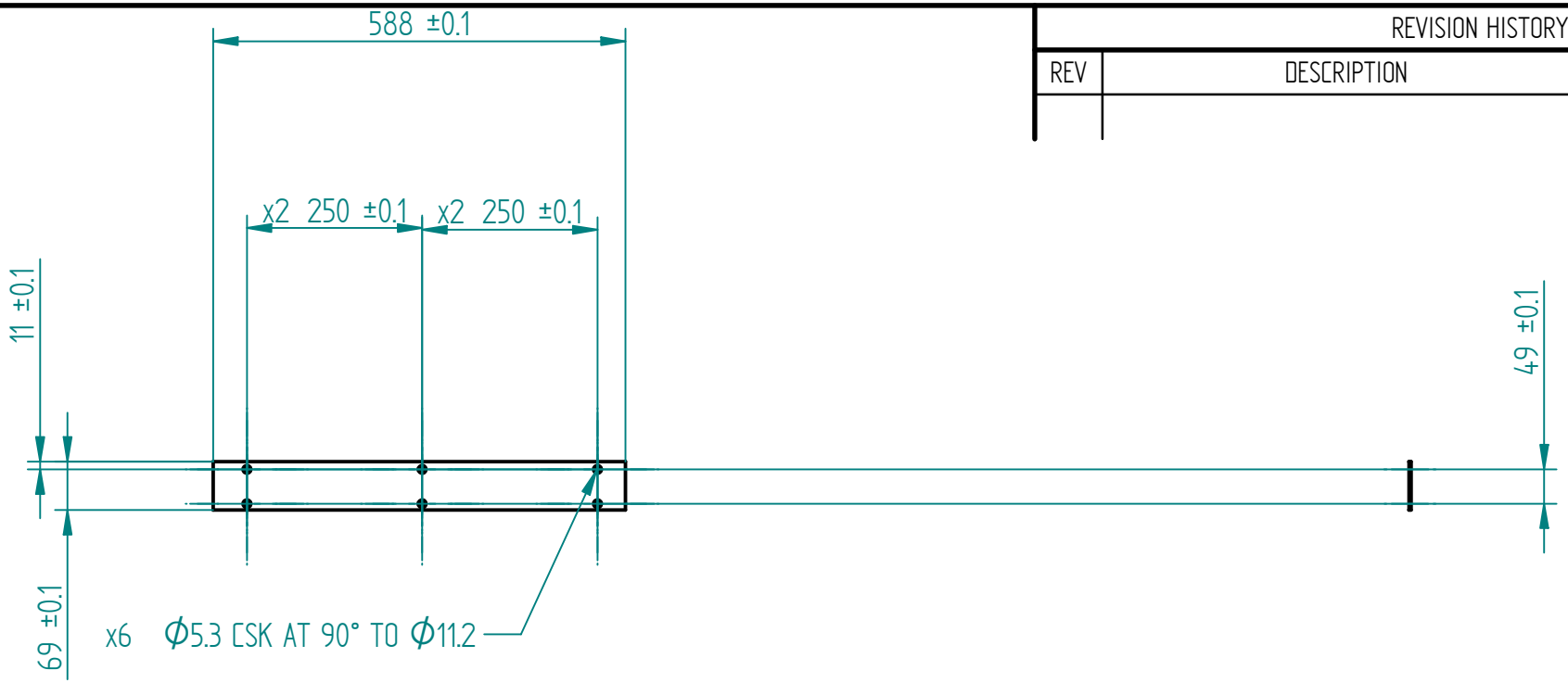

REVISION HISTORY			
REV	DESCRIPTION	DATE	APPROVED

Material – Aluminum
Number of Parts – 1
Texture – Matt Black

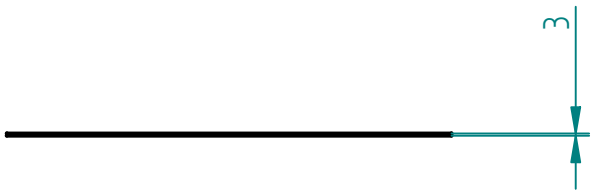

	NAME	DATE
DRAWN	Elad Rind	06/11/07
CHECKED		
ENG APPR		
MGR APPR		

UNLESS OTHERWISE SPECIFIED
DIMENSIONS ARE IN MILLIMETERS
ANGLES ±X.X°
2 PL ±X.XX 3 PL ±X.XXX

SOLID EDGE
UGS - The PLM Company

TITLE

SIZE	DWG NO	REV
A4		

FILE NAME: Draft.dft

SCALE: 1:10	WEIGHT:	SHEET 3 OF 18

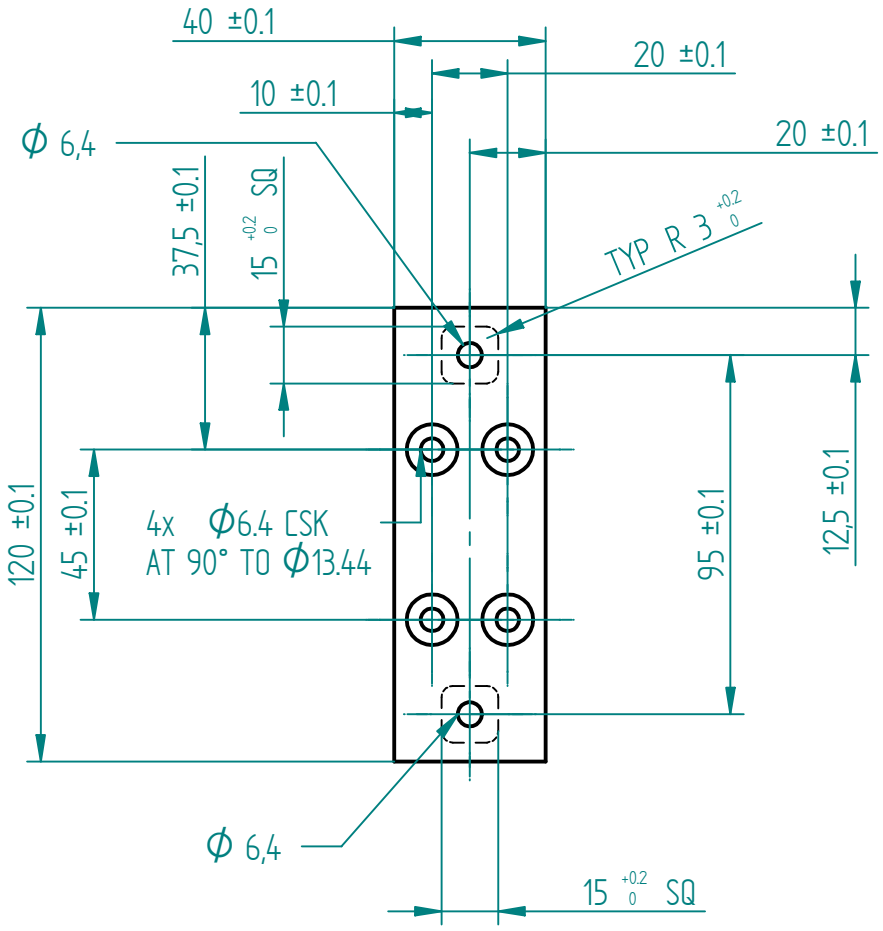

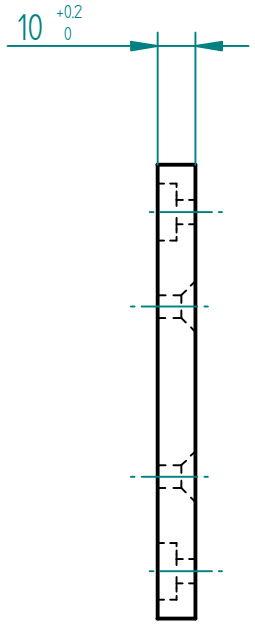

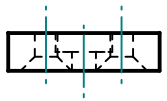

REVISION HISTORY			
REV	DESCRIPTION	DATE	APPROVED

Material – Aluminum
Number of Parts – 2
Texture – Matt Black

	NAME	DATE
DRAWN	Elad Rind	06/11/07
CHECKED		
ENG APPR		
MGR APPR		

UNLESS OTHERWISE SPECIFIED
DIMENSIONS ARE IN MILLIMETERS
ANGLES ±X.X°
2 PL ±X.XX 3 PL ±X.XXX

SOLID EDGE
UGS - The PLM Company

TITLE

SIZE	DWG NO	REV
A4		

FILE NAME: Draft.dft

SCALE: 1:2	WEIGHT:	SHEET 4 OF 18

REVISION HISTORY			
REV	DESCRIPTION	DATE	APPROVED

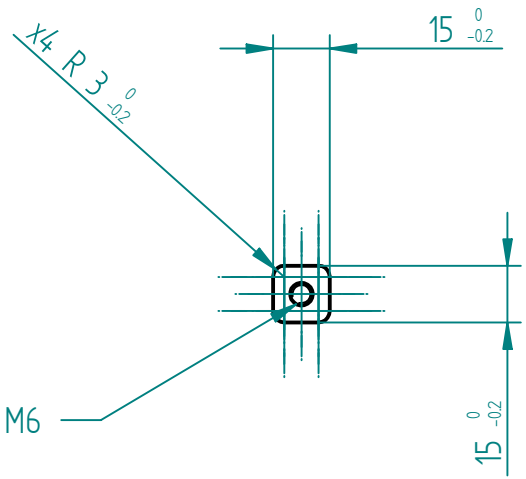

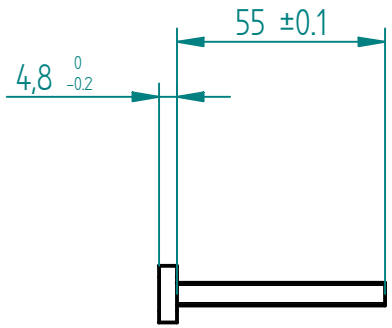

Material – Aluminum
Number of Parts – 4
Texture – Matt Black

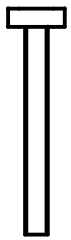

	NAME	DATE
DRAWN	Elad Rind	06/11/07
CHECKED		
ENG APPR		
MGR APPR		

UNLESS OTHERWISE SPECIFIED
DIMENSIONS ARE IN MILLIMETERS
ANGLES ±X.X°
2 PL ±X.XX 3 PL ±X.XXX

SOLID EDGE
UGS - The PLM Company

TITLE

SIZE	DWG NO	REV
A4		

FILE NAME: Draft.dft

SCALE: 1:2	WEIGHT:	SHEET 5 OF 18

REVISION HISTORY			
REV	DESCRIPTION	DATE	APPROVED

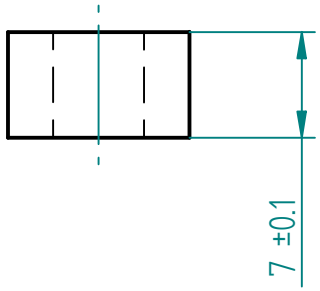

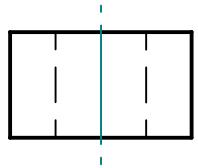

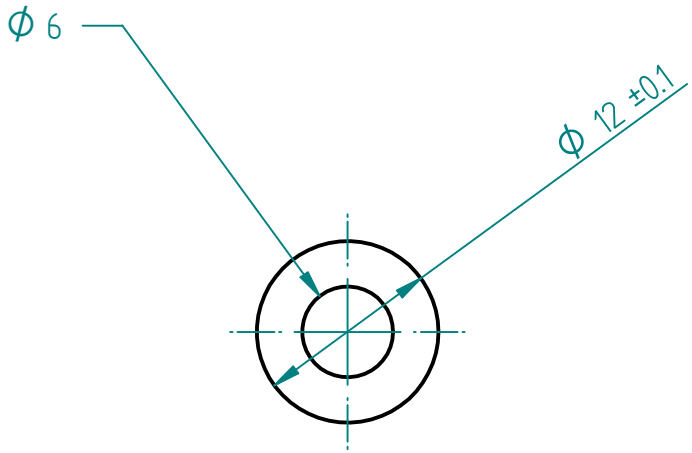

Material – Aluminum
Number of Parts – 6
Texture – Matt Black

	NAME	DATE
DRAWN	Elad Rind	06/11/07
CHECKED		
ENG APPR		
MGR APPR		

UNLESS OTHERWISE SPECIFIED
DIMENSIONS ARE IN MILLIMETERS
ANGLES ±X.X°
2 PL ±X.XX 3 PL ±X.XXX

SOLID EDGE
UGS - The PLM Company

TITLE

SIZE	DWG NO	REV
A4		

FILE NAME: Draft.dft

SCALE: 2:1	WEIGHT:	SHEET 6 OF 18

REVISION HISTORY			
REV	DESCRIPTION	DATE	APPROVED

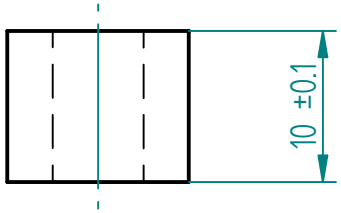

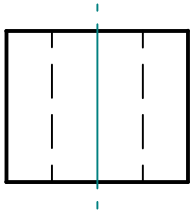

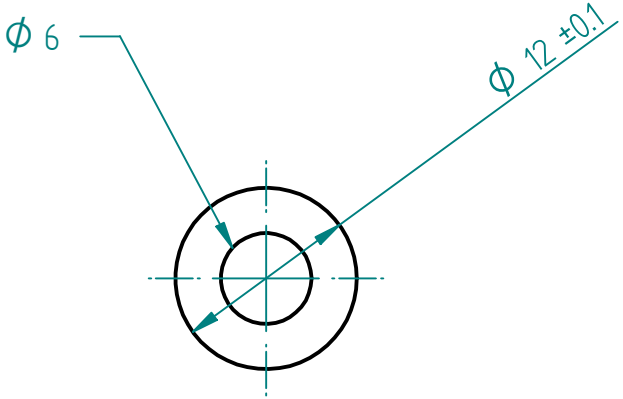

Material – Aluminum
Number of Parts – 6
Texture – Matt Black

	NAME	DATE
DRAWN	Elad Rind	06/11/07
CHECKED		
ENG APPR		
MGR APPR		

UNLESS OTHERWISE SPECIFIED
DIMENSIONS ARE IN MILLIMETERS
ANGLES ±X.X°
2 PL ±X.XX 3 PL ±X.XXX

SOLID EDGE
UGS - The PLM Company

TITLE

SIZE	DWG NO	REV
A4		

FILE NAME: Draft.dft

SCALE: 2:1	WEIGHT:	SHEET 7 OF 18

REVISION HISTORY			
REV	DESCRIPTION	DATE	APPROVED

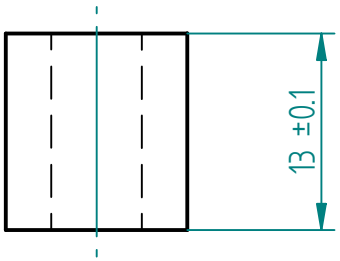

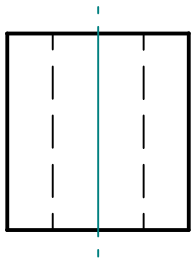

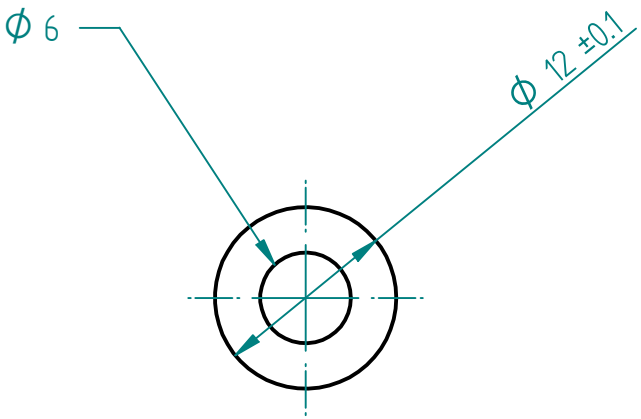

Material – Aluminum
Number of Parts – 6
Texture – Matt Black

	NAME	DATE
DRAWN	Elad Rind	06/11/07
CHECKED		
ENG APPR		
MGR APPR		

UNLESS OTHERWISE SPECIFIED
DIMENSIONS ARE IN MILLIMETERS
ANGLES ±X.X°
2 PL ±X.XX 3 PL ±X.XXX

SOLID EDGE
UGS - The PLM Company

TITLE

SIZE	DWG NO	REV
A4		

FILE NAME: Draft.dft

SCALE: 2:1	WEIGHT:	SHEET 8 OF 18

REVISION HISTORY			
REV	DESCRIPTION	DATE	APPROVED

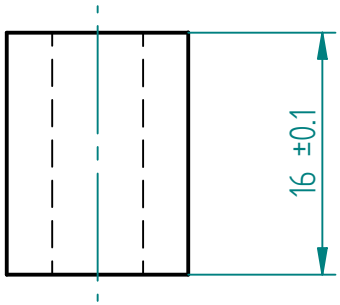

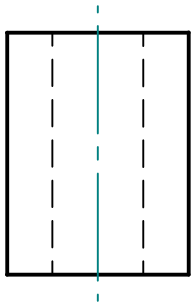

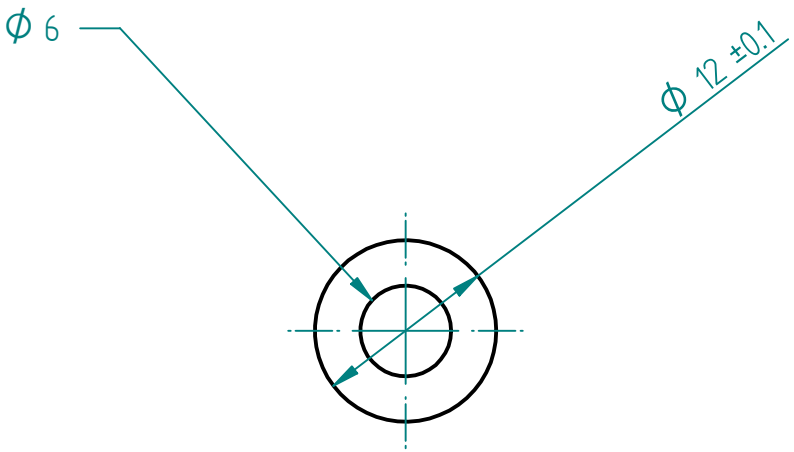

Material – Aluminum
Number of Parts – 6
Texture – Matt Black

	NAME	DATE
DRAWN	Elad Rind	06/11/07
CHECKED		
ENG APPR		
MGR APPR		

UNLESS OTHERWISE SPECIFIED
DIMENSIONS ARE IN MILLIMETERS
ANGLES ±X.X°
2 PL ±X.XX 3 PL ±X.XXX

SOLID EDGE
UGS - The PLM Company

TITLE

SIZE	DWG NO	REV
A4		

FILE NAME: Draft.dft

SCALE: 2:1	WEIGHT:	SHEET 9 OF 18

REVISION HISTORY			
REV	DESCRIPTION	DATE	APPROVED

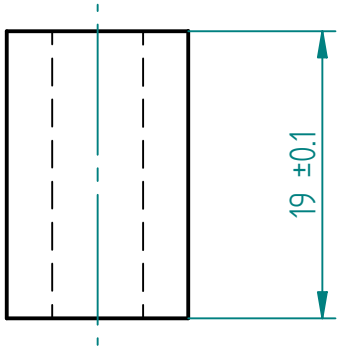

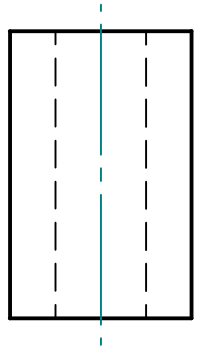

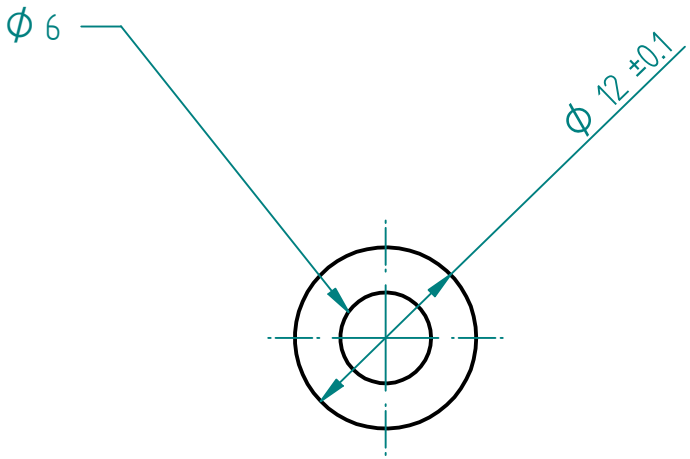

Material – Aluminum
Number of Parts – 6
Texture – Matt Black

	NAME	DATE
DRAWN	Elad Rind	06/11/07
CHECKED		
ENG APPR		
MGR APPR		

UNLESS OTHERWISE SPECIFIED
DIMENSIONS ARE IN MILLIMETERS
ANGLES ±X.X°
2 PL ±X.XX 3 PL ±X.XXX

SOLID EDGE
UGS - The PLM Company

TITLE

SIZE	DWG NO	REV
A4		

FILE NAME: Draft.dft

SCALE: 2:1	WEIGHT:	SHEET 10 OF 18

REVISION HISTORY			
REV	DESCRIPTION	DATE	APPROVED

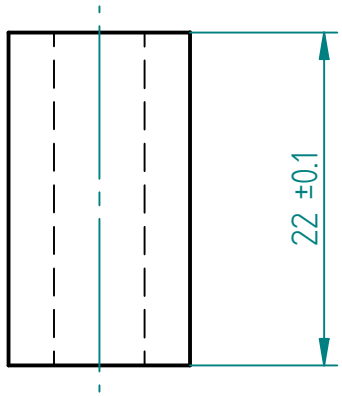

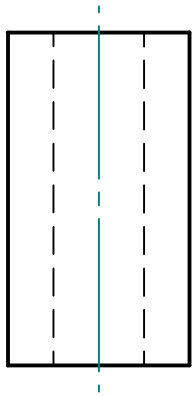

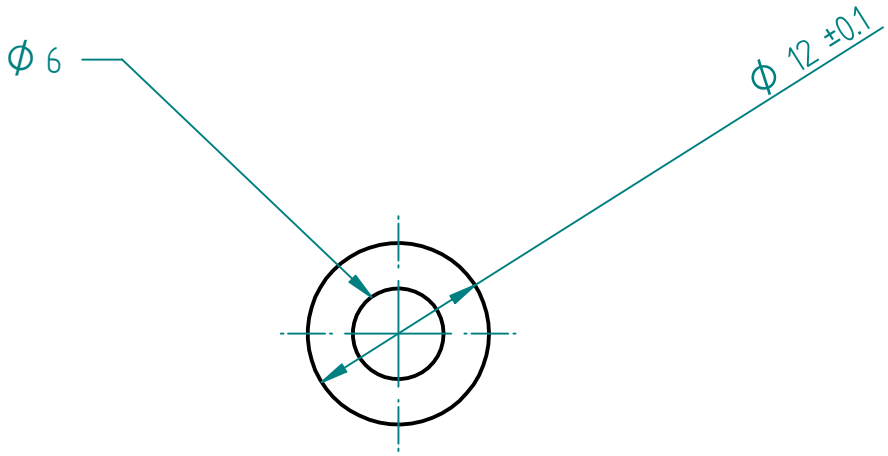

Material – Aluminum
Number of Parts – 6
Texture – Matt Black

	NAME	DATE
DRAWN	Elad Rind	06/11/07
CHECKED		
ENG APPR		
MGR APPR		

UNLESS OTHERWISE SPECIFIED
DIMENSIONS ARE IN MILLIMETERS
ANGLES ±X.X°
2 PL ±X.XX 3 PL ±X.XXX

SOLID EDGE
UGS - The PLM Company

TITLE

SIZE	DWG NO	REV
A4		

FILE NAME: Draft.dft

SCALE: 2:1	WEIGHT:	SHEET 11 OF 18

REVISION HISTORY			
REV	DESCRIPTION	DATE	APPROVED

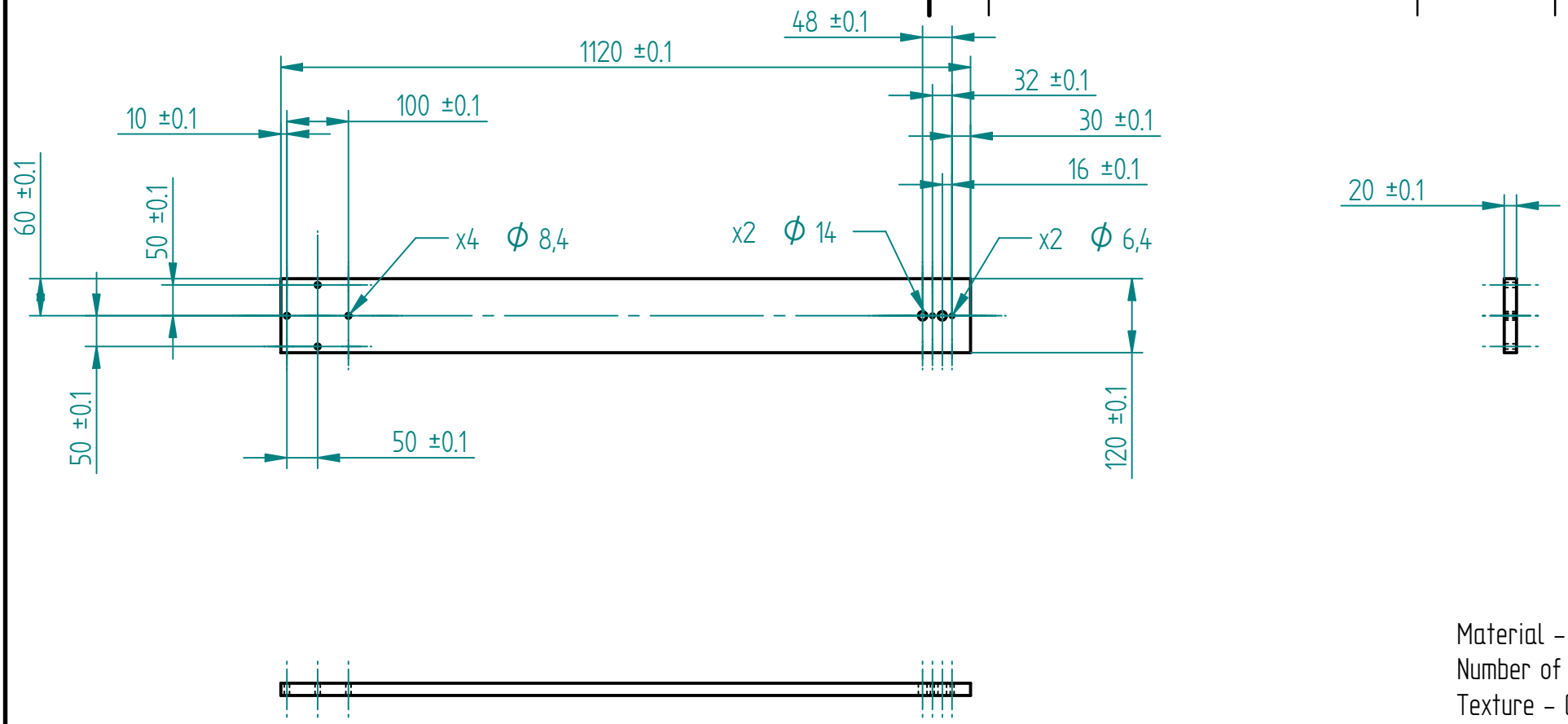

Material – Aluminum
Number of Parts – 1
Texture – Clean

	NAME	DATE
DRAWN	Elad Rind	06/11/07
CHECKED		
ENG APPR		
MGR APPR		

UNLESS OTHERWISE SPECIFIED
DIMENSIONS ARE IN MILLIMETERS
ANGLES ±X.X°
2 PL ±X.XX 3 PL ±X.XXX

SOLID EDGE
UGS - The PLM Company

TITLE

SIZE	DWG NO	REV
A4		

FILE NAME: Draft.dft

SCALE: 1:10	WEIGHT:	SHEET 12 OF 18

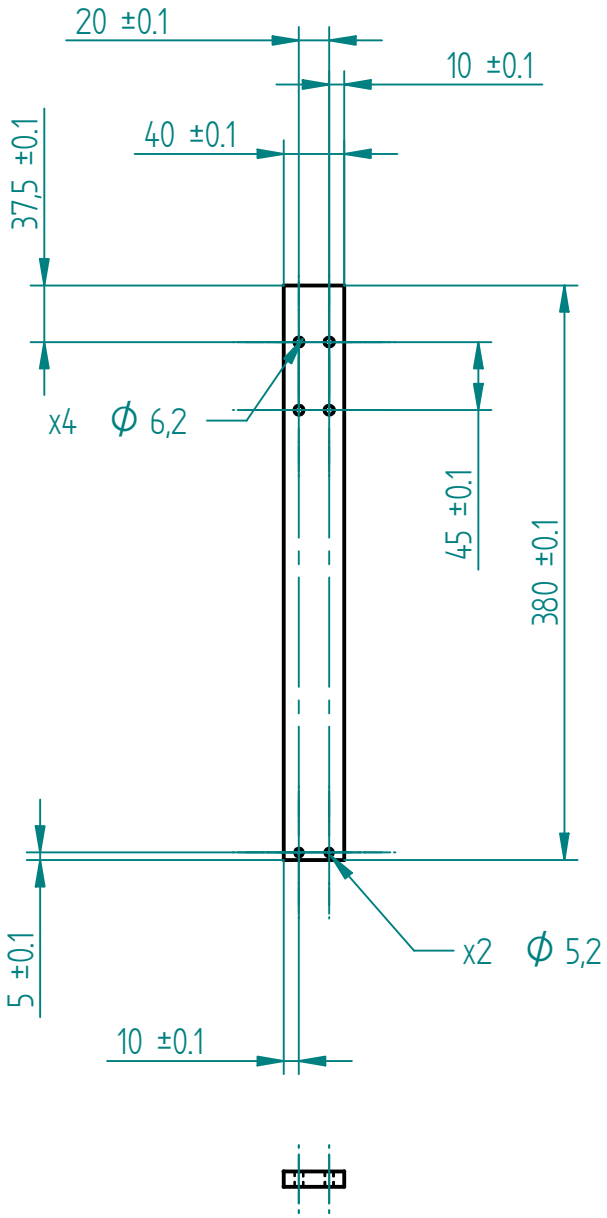

REVISION HISTORY			
REV	DESCRIPTION	DATE	APPROVED

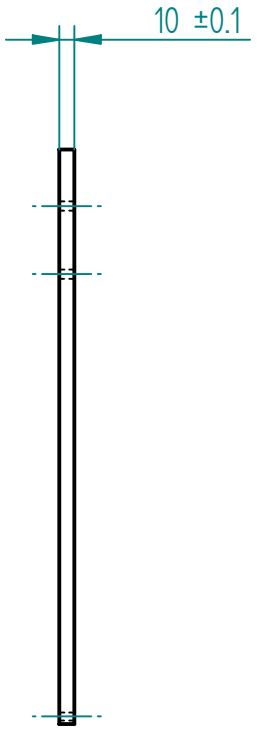

Material – Aluminum
Number of Parts – 2
Texture – Matt Black

	NAME	DATE
DRAWN	Elad Rind	06/11/07
CHECKED		
ENG APPR		
MGR APPR		

UNLESS OTHERWISE SPECIFIED
DIMENSIONS ARE IN MILLIMETERS
ANGLES ±X.X°
2 PL ±X.XX 3 PL ±X.XXX

SOLID EDGE
UGS - The PLM Company

TITLE

SIZE	DWG NO	REV
A4		

FILE NAME: Draft.dft

SCALE: 1:5	WEIGHT:	SHEET 13 OF 18

REVISION HISTORY			
REV	DESCRIPTION	DATE	APPROVED

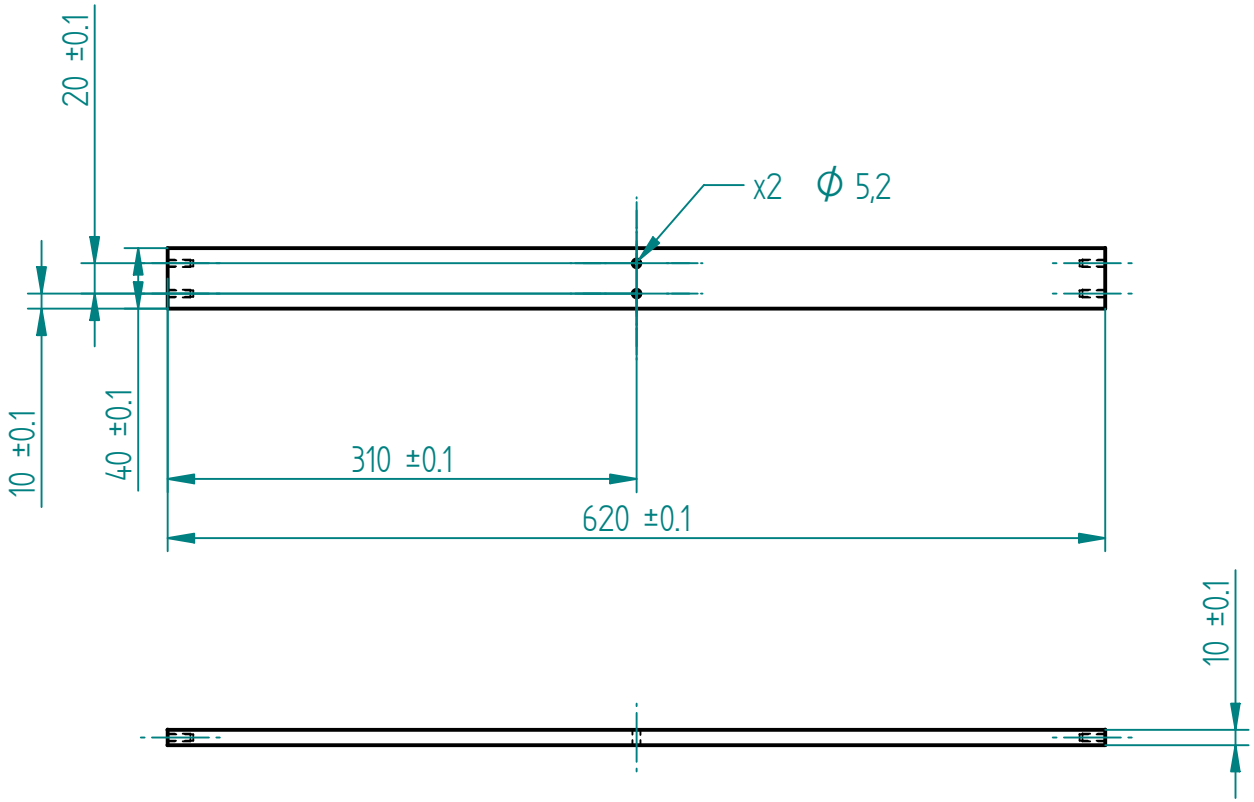

Material - Aluminum
Number of Parts - 1
Texture - Matt Black

	NAME	DATE
DRAWN	Elad Rind	06/11/07
CHECKED		
ENG APPR		
MGR APPR		

UNLESS OTHERWISE SPECIFIED
DIMENSIONS ARE IN MILLIMETERS
ANGLES ±X.X°
2 PL ±X.XX 3 PL ±X.XXX

SOLID EDGE
UGS - The PLM Company

TITLE

SIZE	DWG NO	REV
A4		

FILE NAME: Draft.dft

SCALE: 1:5	WEIGHT:	SHEET 14 OF 18

REVISION HISTORY			
REV	DESCRIPTION	DATE	APPROVED

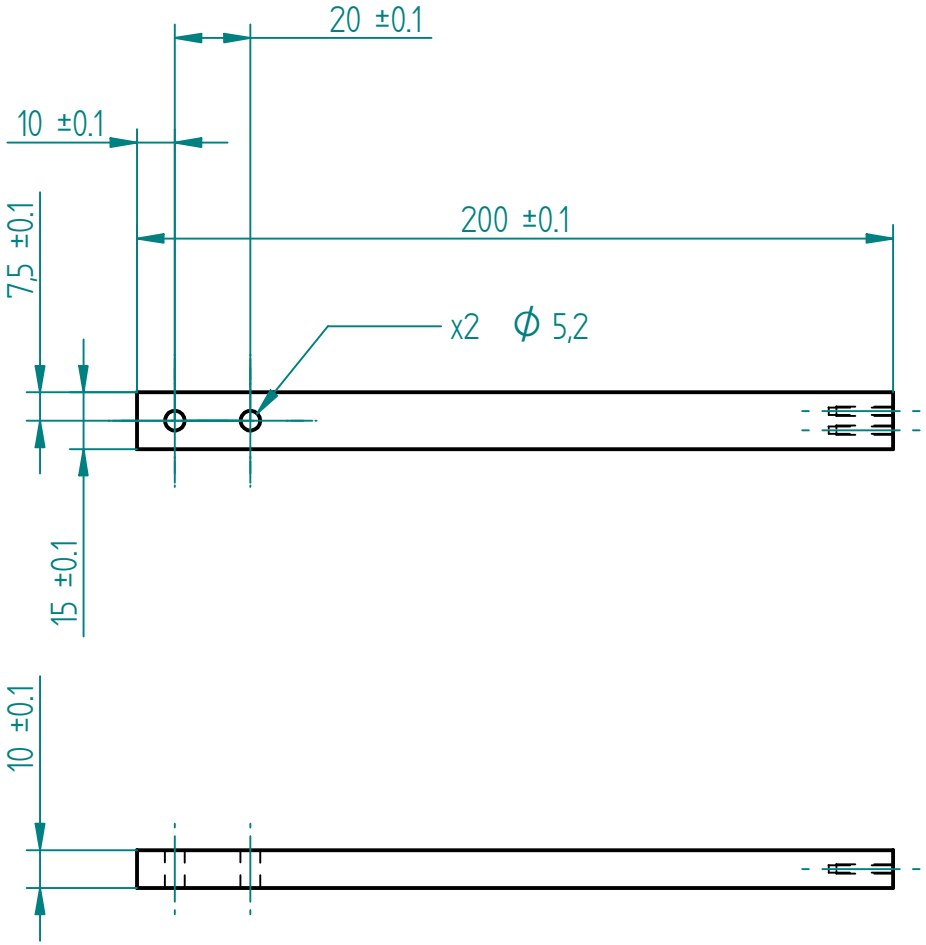

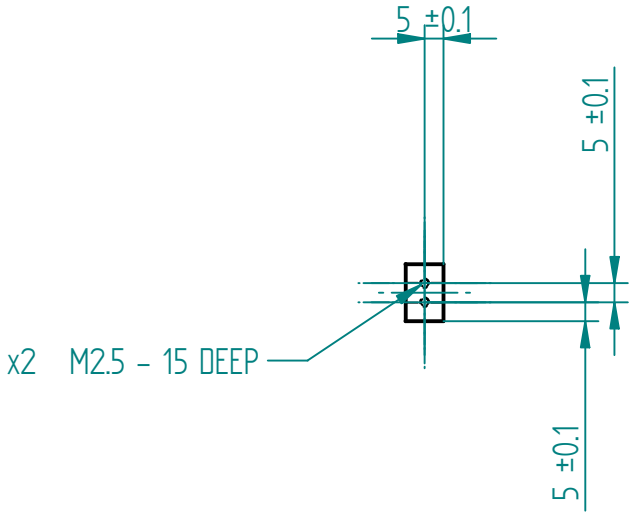

Material – Aluminum
Number of Parts – 1
Texture – Matt Black

	NAME	DATE
DRAWN	Elad Rind	06/11/07
CHECKED		
ENG APPR		
MGR APPR		

UNLESS OTHERWISE SPECIFIED
DIMENSIONS ARE IN MILLIMETERS
ANGLES ±X.X°
2 PL ±X.XX 3 PL ±X.XXX

SOLID EDGE
UGS - The PLM Company

TITLE

SIZE	DWG NO	REV
A4		

FILE NAME: Draft.dft

SCALE: 1:2	WEIGHT:	SHEET 15 OF 18

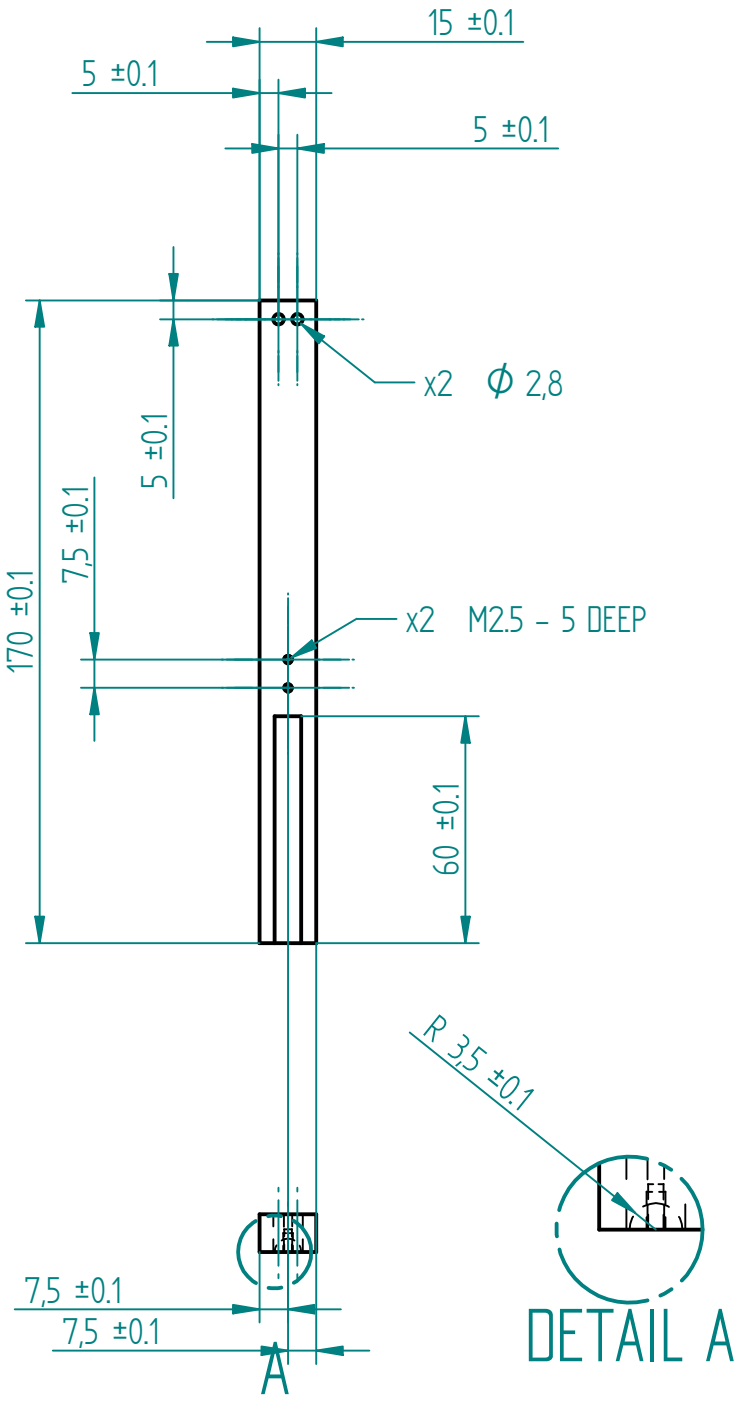

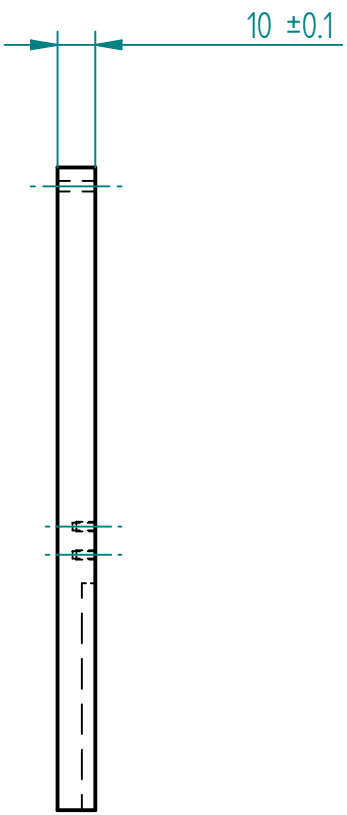

REVISION HISTORY			
REV	DESCRIPTION	DATE	APPROVED

Material – Aluminum
Number of Parts – 1
Texture – Matt Black

	NAME	DATE
DRAWN	Elad Rind	06/11/07
CHECKED		
ENG APPR		
MGR APPR		

UNLESS OTHERWISE SPECIFIED
DIMENSIONS ARE IN MILLIMETERS
ANGLES ±X.X°
2 PL ±X.XX 3 PL ±X.XXX

SOLID EDGE
UGS - The PLM Company

TITLE

SIZE	DWG NO	REV
A4		

FILE NAME: Draft.dft

SCALE:1:5	WEIGHT:	SHEET 16 OF 18

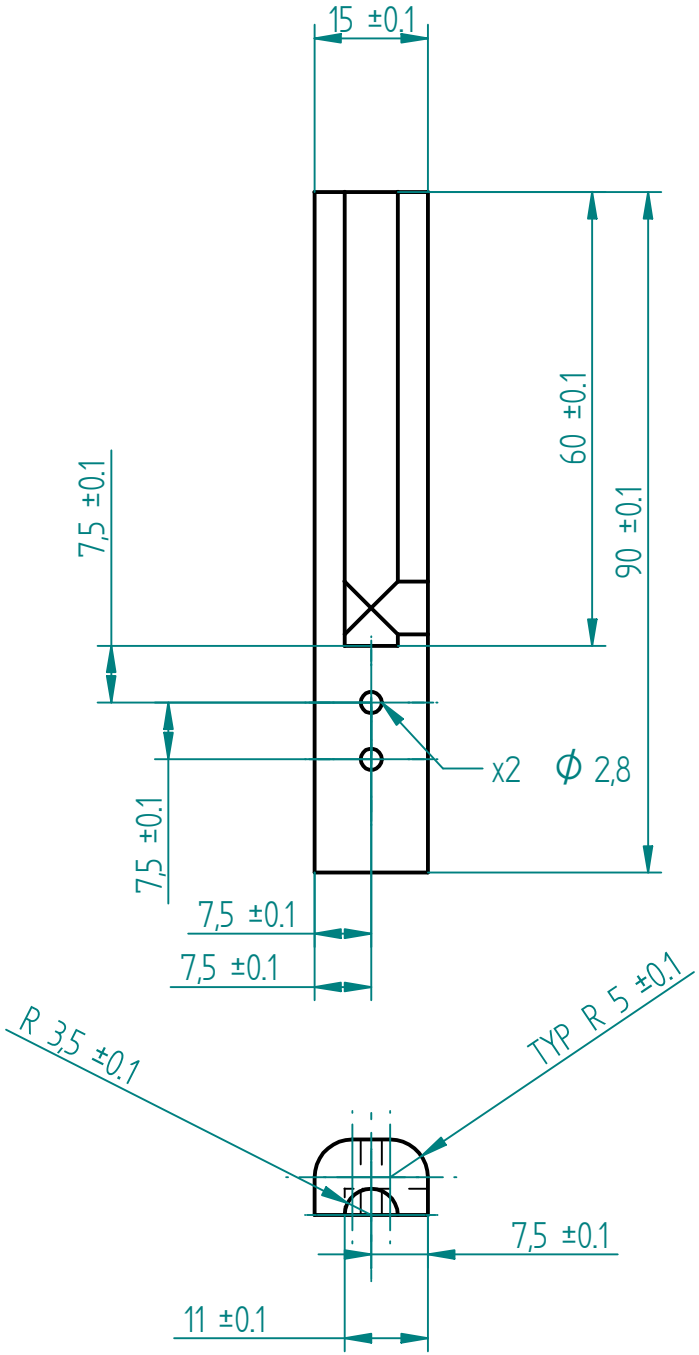

REVISION HISTORY			
REV	DESCRIPTION	DATE	APPROVED

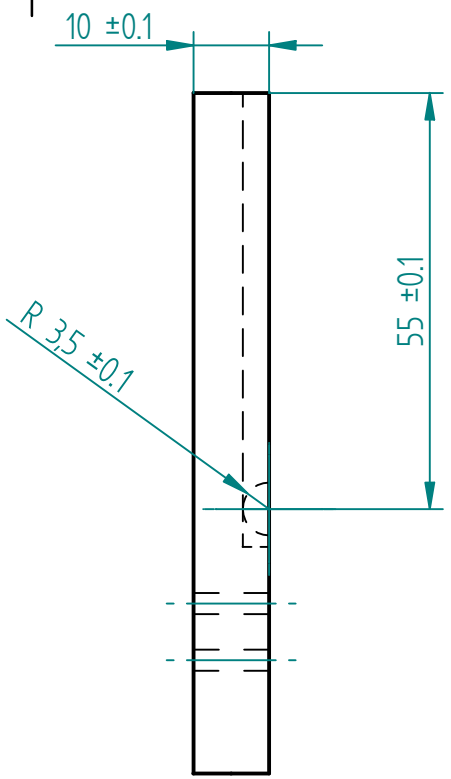

Material – Aluminum
Number of Parts – 1
Texture – Matt Black

	NAME	DATE
DRAWN	Elad Rind	06/11/07
CHECKED		
ENG APPR		
MGR APPR		

UNLESS OTHERWISE SPECIFIED
DIMENSIONS ARE IN MILLIMETERS
ANGLES ±X.X°
2 PL ±X.XX 3 PL ±X.XXX

SOLID EDGE
UGS - The PLM Company

TITLE

SIZE	DWG NO	REV
A4		

FILE NAME: Draft.dft

SCALE: 1:1	WEIGHT:	SHEET 17 OF 18

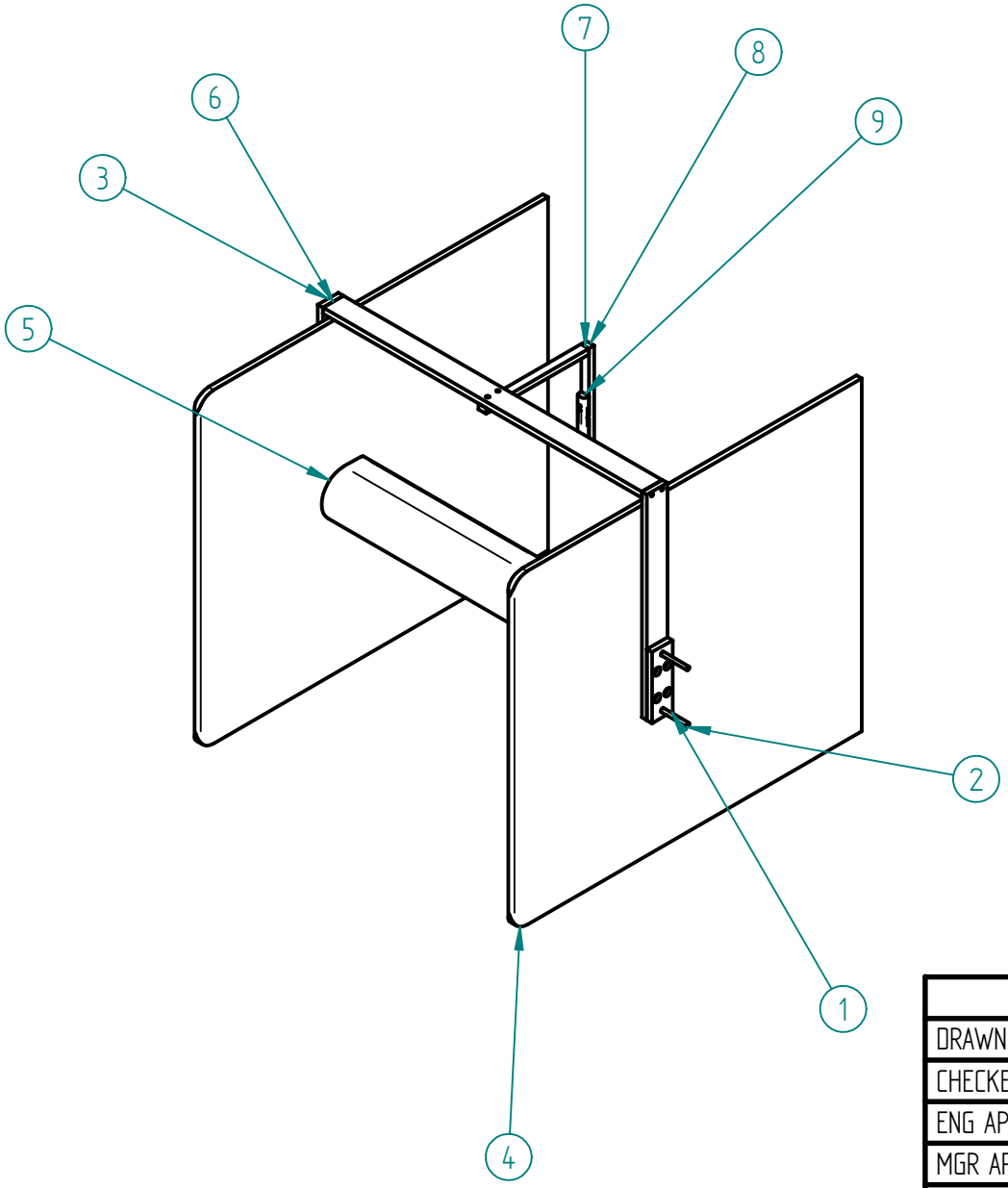

REVISION HISTORY			
REV	DESCRIPTION	DATE	APPROVED

Item Number	Title	Quantity
1	Side Connector	2
2	Screw - 6mm	4
3	Hot Wire Bridge Support	2
4	End Plate	2
5	Frame	1
6	Hot Wire Bridge	1
7	Hot Wire Beam	1
8	Hot Wire Holder - 1	1
9	Hot Wire Holder - 2	1

	NAME	DATE
DRAWN	Elad Rind	06/11/07
CHECKED		
ENG APPR		
MGR APPR		

UNLESS OTHERWISE SPECIFIED
DIMENSIONS ARE IN MILLIMETERS
ANGLES ±X.X°
2 PL ±X.XX 3 PL ±X.XXX

SOLID EDGE
UGS - The PLM Company

TITLE

SIZE	DWG NO	REV
A4		

FILE NAME: Draft.dft

SCALE:	WEIGHT:	SHEET 18 OF 18